# Analysing the limitations of the dual-porosity response during well-tests in naturally fractured reservoirs

# ANALYSING THE LIMITATIONS OF THE DUAL-POROSITY RESPONSE DURING WELL-TESTS IN NATURALLY FRACTURED RESERVOIRS

**D. Egya –** Institute of Petroleum Engineering, Heriot-Watt University, Edinburgh EH14 4AS United Kingdom. doe1@hw.ac.uk

**S. Geiger –** Institute of Petroleum Engineering, Heriot-Watt University, Edinburgh EH14 4AS United Kingdom. S.Geiger@hw.ac.uk

**P. W. M. Corbett –** Institute of Petroleum Engineering, Heriot-Watt University, Edinburgh EH14 4AS United Kingdom. P.W.M.Corbett@hw.ac.uk

**R. March –** Institute of Petroleum Engineering, Heriot-Watt University, Edinburgh EH14 4AS United Kingdom. rmc1@hw.ac.uk

**K. Bisdom –** Delft University of Technology, Department of Geoscience and Engineering – Stevinweg 1, 2628CN Delft (Netherlands). kevin.bisdom@gmail.com

**G. Bertotti –** Delft University of Technology, Department of Geoscience and Engineering – Stevinweg 1, 2628CN Delft (Netherlands). g.bertotti@tudelft.nl

**H. Bezerra** – Department of Earth Sciences – Federal University Rio Grande do Norte (Brazil). bezerrafh@geologia.ufrn.br

## Abstract

Geological reservoirs can be extensively fractured but the well-test signatures observed in the wells may not show a pressure transient response that is representative for naturally fractured reservoirs (NFR), for example one that indicates two distinct pore systems (i.e., the mobile fractures and immobile matrix). Yet, the production behaviour may still be influenced by these fractures. To improve the exploitation of hydrocarbons from NFR, we therefore need to improve our understanding of fluid flow behaviour in fractures.

Multiple techniques are used to detect the presence and extent of fractures in a reservoir. Of particular interest to this work is the analysis of well test data in order to interpret the flow behaviour in an NFR. An important concept for interpreting well test data from an NFR is the theory of dual-porosity model. However, several studies pointed out that the dual-porosity model may not be appropriate for interpreting well tests from all fractured reservoirs.

This paper therefore uses geological well-testing insights to quantify the limitations of the dual-porosity model interpretation of well-test data from Type II and III NFR of Nelson's classification. To achieve this, we apply a geoengineering workflow with Discrete Fracture Matrix (DFM) modelling techniques and unstructured-grid reservoir simulations to generate synthetic pressure transient data in both idealised fracture geometries and real fracture networks mapped in an outcrop of the Jandaira Fomation. We also present key reservoir features that account for the classic V-shape pressure derivatives response in NFR. These include effects of fracture skin, a very tight matrix permeability and wells intersecting a minor, unconnected fracture close to a large fracture or fracture network. Our findings apply to both connected and disconnected fracture networks.


Many sedimentary formations, as well as basement reservoirs, contain naturally occurring fractures, and hence NFR account for a significant amount of the remaining conventional hydrocarbon across

the globe (Bourbiaux 2010; Lemonnier & Bourbiaux 2010b; Spence *et al.* 2014). Many operating companies now follow the advice that "all reservoirs should be considered fractured until proven otherwise" (Narr *et al.* 2006). This approach is driven by the fact that fractures often have an adverse impact on hydrocarbon production, leading to early water breakthrough, irregular drainage and sweep patterns, and low recovery factors as often much of the hydrocarbons are left behind in the less permeable rock matrix (Gilman & Kazemi 1983; Firoozabadi 2000). To improve the exploitation of hydrocarbons from this type of reservoir, we need to improve our understanding of the nature and behaviour of the fractures and the degree to which they influence reservoir performance early during the field development. This knowledge enables us to develop suitable field development strategies for NFR, such as the positioning of wells, planning of water flooding and improved oil recovery (IOR) / enhanced oil recovery (EOR) methods, (*e.g.* Beliveau *et al.* 1993; Wei *et al.* 1998; Nelson 2001; Fernø 2012).

Multiple geological, petrophysical, and geophysical techniques including the use of outcrop analogues, seismic attributes, log data (including image logs), production data, geomechanical simulations, and reservoir simulations are typically integrated to first detect the presence and extent of fractures in a reservoir; secondly to characterise and model the fractures; lastly to understand whether the fractures enhance production or provide barriers to fluid flow (Spence *et al.* 2014).

Pressure transient data obtained during well-testing provides can offer important information as to whether a reservoir is fractured or not and can identify flow behaviours, especially during the appraisal and development stage (*e.g.* Earlougher 1977; Bourdet 2002). A key concept for interpreting NFR from well test data is the theory of the dual-porosity model (also sometimes referred to as the double-porosity model, *e.g.* Warren & Root 1963; Moench 1984; Gringarten 1984 & 1987; Chen 1989). This model was first proposed by Barenblatt *et al.* (1960) to simulate flow behavoir in fractured reservoirs and developed by Warren & Root (1963) to model pressure transient behaviour in well test from NFR. It has been the industry standard for modelling NFR and interpreting well-test data from NFR for more than 50 years (Chen 1989; Cinco-Ley 1996; Bourdet 2002; Syihab 2009;

Lemonnier & Bourbiaux 2010a; Kuchuk & Biryukov 2014 and Morton *et al.* 2015). The dual-porosity model consists of two regions with distinct porosities and permeability, representing the matrix and fractures within the formation (Figure 1a and b). The matrix constitutes the region with negligible flow capacity but significant pore volume that is providing the primary porosity to the reservoir system. The fracture system provides the main path and capacity for fluid flow from the formation to the well but has low porosity. The dual-porosity model only considers matrix-fracture and fracture-fracture flow but not matrix-matrix exchange. However, this model can be extended to a dual-permeability model, which assumes that the matrix is permeable and allows for flows between matrix blocks. (Lemonnier & Bourbiaux 2010a, b).

**Figure 1**

Warren & Root (1963) introduced the first technique for identification and interpretation of the NFR. Their theoretical results, which were reproduced by Kazemi (1969), (see Figure 2), show that the pressure drop or build up on a semilog plot is characterized by two parallel straight lines related to the two distinct regions (dual porosities) in the reservoir. The first straight line (A) indicates the pseudo-radial flow from the fracture system. This is followed by the transition period (B) when depleted fractures are recharged by the matrix discharge until both systems attain equilibrium. Pressure stabilization in the two systems yield the second straight line (radial flow), (C). The development of the pressure derivatives and type-curves (Bourdet & Gringarten 1980; Bourdet *et al.* 1983; Gringarten 1987; Bourdet *et al.* 1989) provide more efficient ways to diagnose dual-porosity behaviour and to determine permeability-thickness (kh) and fracture volumes in NFR. They also aid the identification of other flow regimes that are not discernible by the semilog plot (Figure 2). On the log-log analysis plot (Figure 3), the Warren & Root dual-porosity model is depicted by a dual-porosity “dip” (V-shape) – a minimum on the pressure derivative profile (B) sandwiched between the first stabilisation (corresponding to a period of flow from the fracture system, A) and second stabilisation (the combined flow from both fracture and matrix system, C).

**Figure 2**

**Figure 3**

Nelson's (2001) classified NFR into four categories depending on the contribution of fractures to the reservoir quality and recovery:

Type I: Fractures provide the required reservoir porosity and permeability to produce a reservoir.

Type II: Fractures provide the essential reservoir permeability to produce a reservoir.

Type III: Fractures contribute permeability to an already producible reservoir.

Type IV: Fractures contribute no additional porosity or permeability but create significant barriers to a reservoir flow.

Based on the above categories, the assumptions inherent to the Warren & Root dual-porosity model are only applicable to Type II of the Nelson's classification where the matrix is stagnant but not all dual-porosity (fracture-matrix) systems.

Several studies, including Wei *et al.* (1998), Corbett *et al.* (2012), Morton *et al.* (2012 & 2013), Agada *et al.* (2014), Kuchuk & Biryukov 2014, Morton *et al.* (2015), Kuchuk & Biryukov (2015) and Egya *et al.* (2016 & 2017) have demonstrated that the pressure behaviour in an NFR can be notably different from the theoretical dual-porosity behaviour predicted for of a heavily fractured NFR with well-connected fracture networks. In these cases, the pressure responses do not exhibit the classical dual-porosity behaviour and hence the use of the Warren & Root (1963) dual-porosity model may not be appropriate for identification and interpretation of all NFR, particularly for moderately and/or discretely fractured reservoirs. This raises the important question of what properties of the fracture network cause the dual-porosity signal to be absent in some NFR and to be present in others. Since the location, orientation, and connectivity of fractures are very difficult to quantify directly and unambigously in the reservoir, linking known properties of the fracture network to the dynamic response during a well-test remains elusive.

Traditionally, outcrop analogue data has been used for fracture characterisation as they allow for a more direct and detailed observation of the key geological features and principal reservoir properties that could control reservoir performance (Seers & Hodgetts 2013; Howell *et al.* 2014; Geiger & Matthäi 2014). This characterisation typically focuses on the static properties and may be difficult to be scaled and linked to possible subsurface dynamic behaviours. However, new simulation approaches that employ unstructured grids enable us to model mapped outcrop fracture patterns, together with petrophysical data that is representative for a given subsurface reservoir. This way, a numerical simulation model allows us to understand how fractures impact flow behaviours and how this behaviour could be upscaled (Wilson *et al.* 2011; Geiger & Matthai, 2014). The numerical approach is often termed the Discrete Fracture and Matrix (DFM) method (*e.g.* Bogdanov *et al.* 2003; Karimi-Fard *et al.* 2004; Kim & Deo, 2000), as it enables us to explicitly represent the structure and geometry of both, fracture network and rock matrix, in the flow simulations. Applications of the DFM approach that employed outcrop-based fracture patterns include, but are not limited to, single-phase upscaling of multi-scale fracture networks (*e.g.* Matthäi & Belayneh 2004; Ahmadov *et al.* 2007; Zhou *et al.* 2014; Hardebol *et al.* 2015; Bisdom *et al.* 2016), and simulating synthetic well-test signals in fractured formations (Matthäi & Roberts 1996; Corbett *et al.* 2012). Others applications are quantifying the characteristics of heat flow in geothermal systems (Geiger & Emmanuel 2010) and contaminant transport in fractured aquifers (Geiger & Emmanuel 2010; Edery *et al.* 2016), or the analysing multi-phase flow displacement processes in fractured sedimentary formations (*e.g.* Agar *et al.* 2010; Belayneh *et al.* 2006; 2007; 2009; Geiger *et al.* 2009; 2013).

In this study, we will use DFM and unstructured-grid reservoir simulation technologies in combination with multi-scale fracture patterns from outcrop data, and apply a geoengineering workflow (Corbett *et al.* 2012), to quantify how fracture network characteristics, matrix properties, and well-locations impact the pressure transient behaviour observed in well-tests. The results then allow us to quantify in a rigorous and systematic way when and why the assumptions inherent to the dual-porosity model break down when interpreting well-test data from NFR. Firstly, we review the

basic theory of well testing in NFR. We then discuss the geoengineering workflow used in this study and describe the available field data. This is followed by a brief description on how our simulation models are generated and validated. Finally, we present simulation results and observations and finally the conclusions. This paper deals with natural fractures with Type II and III properties of Nelson's (2001) classification. Modelling of hydraulic fractures and vugs are out of the scope of this study. Furthermore, uniform fracture conductivity (either finite or infinite) are assumed in all fracture configurations presented.

## Theory of Well-Testing in a NFR

The dual-porosity model of Warren & Root (1963) model assumes a continuum approach in which matrix and fracture systems are considered to be continuous and uniform throughout the reservoir. Two characteristic parameters control the deviation of the dual-porosity systems from the homogeneous reservoir. These parameters are the storativity ratio and interporosity flow coefficient. The storativity ratio $\omega$ is defined as the ratio of fluid stored in fracture system to that of the total reservoir system,

$$\omega = \frac{\varphi_f C_f}{\varphi_f C_f + \varphi_m C_m}, \tag{1}$$

where $\varphi_f$, $\varphi_m$, $C_f$ and $C_m$ denote fracture porosity, matrix porosity, fracture compressibility and matrix compressibility respectively.

The interporosity flow coefficient $\lambda$ reflects the contrast between the permeability of the matrix and fracture – *i.e.*, it is a measure of the ability of the fluid to flow from the matrix into the fractures,

$$\lambda = \alpha {r_w}^2 \frac{k_m}{k_f}, \tag{2}$$

where $r_w$, $k_m$and $k_f$ denote well radius, matrix permeability and fracture permeability respectively, α is a shape factor that depends on the size and geometry of the matrix.

Warren & Root (1963) also assumed that the interporosity flow from matrix to fractures occurs under pseudo-steady state (PSS) conditions. PSS interporosity flow (PSSIF) supposes that at any given time, the flow and pressure at all points in the matrix blocks is distributed equally, resulting in uniform transfer within the matrix and between the matrix to fracture. Other authors including Odeh (1965), Kazemi *et al.* (1969), Streltsova (1976), and Mavor & Cinco Ley (1979) subsequently shared this assumption. Kazemi (1969), Cinco-Ley & Samaniego (1982), de Swaan (1976), Najurieta (1980), Boulton & Streltsova (1977), Serra *et al.* (1983) and Streltsova (1983) all developed alternatives that overcome the PSSIF assumption and proposed transient interporosity flow (TIF) between fracture and matrix (*i.e.*, the pressure in the matrix blocks can vary locally). This implies that although the response to pressure changes for a fracture intersecting a well is faster in the fracture system compared to the matrix, both systems respond simultaneously at the early time of flow. The TIF assumption argues that PSSIF would be reached only after a considerable period of flow.

Warren & Root's (1963) original model did not consider the effect of wellbore storage and skin. Mavor & Cinco Ley (1979) added the wellbore effects. Bourdet & Gringarten (1980) extended Mavor & Cinco Ley's (1979) wellbore storage effect to the TIF model. Moench (1984) and Cinco-Ley *et al.* (1985) further showed that the early PSSIF regime can be linked to a skin effect (damage at the surface of the blocks) between the matrix and the fractures. Under these restricted inter-porosity flow conditions, the partial plugging of fractures caused by mineralisation or any form of formation damage result in permeability reduction normal to the fracture face thus allowing an impaired flow of fluid discharged from the matrix to the fractures. Both PSSIF and TIF flow conditions have been found in fields and/or presented in the literature (Gringarten 1984; Wei *et al.* 1998; Bourdet 2002; Kuchuk *et al.* 2015), leading to a debate as to which of these assumptions is more reliable and justified in modelling and interpreting NFR. Recent studies suggest that neither form, PSSIF or TIF, of the dual-porosity model assumptions may be adequate to interpret well-test data from certain NFR,

*e.g.* discrete fracture networks (Wei *et al.* 1998; Corbett *et al.* 2012; Morton *et al.* 2012, 2013; Agada *et al.* 2014; Kuchuk & Biryukov 2014, 2015; Morton *et al.* 2015).

## Methodology and Data

### *Geoengineering Workflow*

In order to appropriately evaluate the flow behaviour of fractures on pressure transient data from NFR, we adopted the geoengineering workflow of Corbett *et al.* (2012, see Figure 4). At the heart of the geoengineering workflow lies the numerical simulation of the diffusivity equation,

$$\phi C_t \frac{\partial p}{\partial t} = \nabla . \left[ \frac{\boldsymbol{k}(\boldsymbol{x})}{\mu} \nabla p \right], \tag{3}$$

for given reservoir properties and reservoir geometries where $p$, $t$ and $C_t$ denote pressure, time and total compressibility respectively. $\boldsymbol{k}(\boldsymbol{x})$ and $\mu$ denote the (spatially varying) permeability tensor and fluid viscosity respectively.

From the solution of the diffusivity equation (Eq. 3), we can obtain synthetic pressure transient data at wells that are placed in selected locations in the reservoir. Next we can correlate the observed pressure data to routine Pressure Transient Analysis (PTA) with the known input parameters (*e.g.* fracture orientation and connectivity) in the reservoir model to understand how the dynamic reservoir behaviour is impacted by natural fractures. The workflow can be summarised in the following steps (see Figure 4):

1. Build a detailed synthetic geological model comprising a mapped fracture network (from an outcrop analogue),

2. Use petrophysical properties from logs for the matrix that is representative of a subsurface reservoir.
3. Represent the geological model in a reservoir simulation model that employs unstructured grids so that the fractures can be preserved explicitly.
4. Numerically simulate drawdown for a wide range of possible reservoir parameters and well locations.
5. Analyse the resulting numerical pressure transient data in a well-test package for PTA.
6. Estimate the effective reservoir parameters for the simulation model.
7. Correlate the pressure transient to the known geological features of the reservoir model. Where analysis disagrees with model input, make necessary changes to improve performance and correlation.

**Figure 4**

We use the geoengineering workflow with the DFM approach that is available in the open source Matlab Reservoir Simulation Toolbox MRST (Lie *et al.* 2012) to solve Equation (3) numerically explicitly resolve the fractures in the reservoir models, and evaluate the effect of geometric arrangements of the fracture network as well as well locations on the pressure transient signals[1]. MRST offers a range of different discretisation methods. Here, we employ the PEpendicular Bisector (PEBI) method in MRST, which has proven to be efficient, robust and accurate when discretising complex realistic fractures networks (Sun *et al.* 2015). The conditions for accurate PEBI simulations are that the permeabilities are isotropic and permeability orthogonality is guaranteed. However, the main advantage of the PEBI approach is its flexibility, enabling the grids to conform to complex geometric features, including fractures and radial gridding around the wells, whilst resolving the early time transients (Zheng *et al.* 2007).

[1] The input files can be downloaded from: http://carbonates.hw.ac.uk

***PEBI Gridding and Numerical Modelling***

The PEBI gridding workflow used in this study is illustrated in Figure 5. Fracture traces, well locations, and domain boundaries are represented in the form of linear coordinates. Edges are then delineated by creating a planar straight line graph (PSLG) containing a set of fractures vertices and adjoining edges (Figure 5a). The PSLG provides the input for a constrained Delaunay triangulation (Figure 5b) that honours the original model geometry (Shewchuck, 2002). The resulting triangulation forms the basis on which the complementary PEBI grid is generated such that the centres of the PEBI cells correspond to the nodes of triangular elements (Figure 5c). Finally, the 2D PEBI (Figure 5d – without the drawn PSLG) grid is extruded vertically, resulting in a 2.5D reservoir simulation grid that is horizontally unstructured but vertically structured (Mallison *et al.* 2010; Lie 2015; Sun *et al.* 2015). It is often referred to as 2.5D rather than 3D because the geology/geometry does not change in the third dimension. Throughout this work, we assume that the thickness of the formation is small compared to its lateral extent, and hence no variations in structure occur in the third dimension. Furthermore, the grid around the wells and fractures was locally refined to ensure that steep pressure gradients near wells and, at early time, near the fracture-matrix interfaces, can be preserved accurately.

**Figure 5**

To enable this grid refinement, a procedure was implemented to improve the quality of the mesh at multiple fracture intersections as well as at asymmetric and low-angle intersections. Various approaches have been used to resolve meshing of complex geometry features including small features, sharp angles in intersection features, multiple features intersection, or non-uniform fracture apertures (Branets *et al.* 2009; Syihab 2009; Mallison *et al.* 2010; KAPPA 2012; Olorode *et al.* 2013; Hyman *et al.* 2014; Bahrainian *et al.* 2015; Sun & Schechter 2015). Here, we developed an algorithm that involves creating a protective area where only one finite element node is allowed at the intersection

and no grid refinement is applied within this area local to the intersection (Figure 5a to 5c)[2]. Note that the image in Figure 5d shows an improved mesh where the PEBI cell is constructed around the initial finite element node and the adjoining cells conform to the defined fracture geometry. In addition, we applied the algorithm of Møyner & Lie (2016) to refine the grid radially around the well, especially in cases where wells are located in the matrix and close to fractures (Figure 5e).

Once the 2.5D reservoir model is constructed, it is populated with representative subsurface petrophysical properties (step 2 in Figure 4 and Table 1), including porosity and permeability that are used as input for flow computations. For simplicity, the reservoir matrix is assumed to be isotropic and homogeneous so that single constant values of petrophysical properties can be used, but heterogeneous matrix properties are possible too. The fractures are assumed to be open (100% porosity), have higher permeabilities than the matrix, and also have uniform properties that do not change as a function of pressure (*i.e.*, the reservoir is stress-insensitive). Fracture permeabilities $k_f$ are computed from the fracture aperture, $a$, using the parallel plate law, *i.e.*, $k_f = a^2/12$. To avoid infeasibly small grid cells in the fracture, we rescaled the fracture permeability and porosity, in case a fracture grid block was wider than the fracture aperture to obtain the correct face transmissibility.

To ensure that numerical artefacts do not impact the simulation results, we tested how grid refinement around the fractures and well, as well as the selection of time-steps, influences the numerical simulations by comparing synthetically generated pressure profiles to and analytical solutions for various levels of grid refinement and time-steps. Based on this analysis, all models use grids that coarsen logarithmically away from the smallest geometric feature (*i.e.*, the gridblocks containing the fractures) and set the maximum grid block size to be four orders of magnitude larger than the smallest grid block in the model. Simulation time-steps are also increased logarithmically to ensure smooth pressure transient profiles. The simulation results were further compared, for simple orthogonal fracture patterns, to a commercial simulator (CMG IMEX).

[2] This code can be downloaded from http://carbonates.hw.ac.uk

***Model validation***

A number of sensitivity studies were completed to validate the accuracy of the modelling methodology, and to make sure that the pressure transient response from the reservoir reflects the physical conditions and are not impacted by numerical dispersion. For the model validation, we ran simulations for matrix model (Table 2, Model 1), single fracture (Table 2, Model 2) and multiple intersecting (multiwing) fractures (Table 2, Model 3) models where the well is located centrally and symmetrically in single fracture and at a bifurcation point for multiwing fractures, respectively (see Figure 7a and 8a). The first set of results are for the homogeneous matrix models with a well located at the centre of a square reservoir block (Figure 6). Each of the graphs in Figure 6 show the main flow regimes (early time wellbore storage, WBS, with slope m = 1; radial flow with m = 0, and late time PSS flow with m = 1, indicating boundary) and captures the sensitivities to changes in reservoir parameters (KAPPA 2012). Figure 6a shows similar pressure derivatives as a function of permeability. However higher values of permeability deviate from pure WBS at earlier times, indicating the reservoir's ability to react faster to production. Changes in porosity (Figure 6b) do not show changes in the stabilisation of the pressure derivative (*i.e.*, during radial flow). Deviations are observed, however, during transition from pure WBS to radial flow and from radial flow to PSS. Given the same reservoir size and properties, changes in porosity are proportional to the time for PSS influence to reach the well. Figure 6c shows that with changes in production rate, the derivative shifts vertically but the pressure profile remains the same. High rates produce proportionately high pressure deviations from the initial pressure, shifting the derivative upwards. The effects of changes in viscosity on pressure derivative is opposite those described above for changes in permeability (Figure 6a).

Next, we performed sensitivity analysis using simple fracture geometries so that our numerical model can be validated with existing analytical solutions (Bourdet 2002). Results for a close-up of the unstructured PEBI grid with refinement around a single fracture intercepted by a well (Figure 7a) are

shown in Figure 7b. From top to bottom on Figure 7b, the flow regimes identified with changes in the conductivity include bilinear flow, m = ¼; linear flow, m = ½ and radial flow, m = 0. Detailed description of the PTA of a single fracture model is provided later in the section "Simulation Results and Observations". Figure 8a shows close-up of the unstructured PEBI grid with refinement around multiwing fractures used to further validate our model. The results (Figure 8b) showing changes in pressure (dashed lines) and the corresponding pressure derivatives (solid lines) for different values of Asymmetry Factors (AF) indicate similar responses to the analytical and semi-analytical solutions of Berumen *et al.* (2000) and Wanjing & Changfu (2014), respectively. The AF measures the well offset from the centre of the fracture. Our simulation results were also validated using CMG IMEX for simple orthogonal fracture patterns. The validation models further provide references for the interpretation of the more complex fracture geometries simulated later.

In all simulation models, a jacket of matrix cells with uniform properties is added to prevent flow in the fractures from interacting with the model boundary (Aljuboori *et al.* 2015). Since the fracture cells are characterised with a high permeability, the pressure response in this medium can propagate very quickly to the model boundary even before the effect of exchange between fractures and the matrix has started. Therefore, it is necessary to prevent the late time boundary effect from interfering with the middle time pressure transient response in our simulations.

**Figure 6**

**Figure 7**

**Figure 8**

***Outcrop Data and other Input Parameters***

The approach of this study is applied to a real outcrop of fracture networks (Figure 9) obtained from the Turonian-Campanian Jandaira carbonate formation, which crops out in large parts of the Potiguar

basin in NE Brazil (Bertotti *et al.* 2017; de Graaf *et al.* 2017). The Jandaira formation is a sub-horizontal formation, dipping on average 3° towards the North, creating exposed pavements with dimensions exceeding several hundred by several hundred meters. These exposures are ideal for multiscale fracture network characterization. Using satellite imagery in combination with drone images and conventional outcrop measurements, more than 18,000 fractures have been mapped in pavements throughout the basin (Bisdom *et al.* 2017).

Although layers with folds and faults are relatively rare, the Jandaira formation is intensely fractured. Based on crosscutting relations between vertical fractures and burial-related horizontal stylolites and the abundance of bed-perpendicular conjugate sets of fractures, most of the fractures are interpreted to have formed at shallow depths during a relatively early phase of burial (Bertotti *et al.* 2017). Outcrop and thin section analyses of fracture infill shows that fractures have shear and opening components, indicating that these are hybrid fractures (Ramsey & Chester 2004; Bertotti *et al.* 2017). The main driving mechanism for fracturing was regional shortening, under a maximum horizontal stress oriented N-S to NE-SW (Bertotti *et al.* 2017; de Graaf *et al.* 2017). As a result, most fractures are oriented N-S and NW-SE, dipping perpendicular to bedding (Bisdom *et al.* 2017).

The E-W striking fractures are barren features in the outcrops, but prior to exhumation these features were tectonic (*i.e.*, bed-perpendicular) stylolites formed in the same N-S to NW-SE regional shortening phase as the fractures (Bertotti *et al.* 2017). Fractures from different orientation families are observed to be mutually crosscutting, providing further evidence for their simultaneous formation. The only hierarchy that is observed in some outcrops is related to fracture size, as smaller fractures terminate against larger fractures.

These burial-related fractures are present at high densities throughout the entire basin, even though there is only limited seismic-scale deformation. These patterns have furthermore been formed under relatively low stresses. There are many carbonate reservoirs that have a similar lack of seismic-scale deformation, where conventional methods such as curvature analysis do not indicate significant

fracturing, but the studies of the Jandaira formation show that high-density fracture patterns may still exist. For this type of fracture networks, there is significant value in having the ability to identify fracture flow from well test data.

Fractures from one of the Jandaira pavements are used in this study (Figure 9). This 400 x 175m pavement has been imaged using a drone, resulting in a georeferenced image from which nearly 2000 fractures were mapped using GIS software (Bisdom *et al.* 2017). Fracture lengths in this pavement from 0.68m to about 90m in length with apertures observed at the outcrop ranging from <0.1mm up to 10mm (Bisdom *et al.* 2016). Bertotti *et al.* (2014) noted that even though the orientation of the structures is preserved, fracture apertures observed in the outcrop are probably not representative of the subsurface conditions and hence we consider variable fracture apertures in our sensitivity study. Like the Jandaira Formation, recent karstification has altered the fracture/joint properties at surface of the outcrop example shown in Figure 1a. For this reason subsurface model parameters are selected in this paper – rather than being measured in the field – with the contrast between matrix and fracture permeability being the important consideration. The variations in fracture density observed in the outcrop in Figure 9 allowed us to evaluate how pressure transients evolve when wells are located in different parts of the fracture network and where the dual-porosity model is valid to interpret the pressure transients. The two insets in Figure 9 indicate locations where smaller-scale models of fractures patterns are taken to simulate disconnected and connected fractures, respectively. The upper inset represents the disconnected fracture network and the lower one the connected fracture network.

The reservoir and fluid properties used in this study are summarised in Table 1. For simplicity, all simulations assume single-phase laminar flow, no gravity effects, a homogenous and isotropic reservoir matrix with uniform thickness, uniform fracture aperture with a single porosity and permeability for the entire fracture network. We also assume layer bound fractures and hence represent the model with the third dimension as a single layer. Well are oriented vertically and fully penetrate the formation and produce at constant rate for any given simulation. Table 2 summarises all simulation scenarios.

**Figure 9**

***Dimensionless Variables***

In this study, the following dimensionless numbers are used to compare and quantify the reservoir properties in the different simulations.

Dimensionless fracture conductivity

$$F_{CD} = \frac{k_f * a}{k_m * l_w} \tag{4}$$

Dimensionless pressure

$$p_D = \frac{k_m h}{141.2 q \mu}[p_0 - p_{wf}(t)] \tag{5}$$

Dimensionless time

$$t_D = \frac{0.0002637 k_m t}{\mu \varphi_m (C_t)_m l_w^2} \tag{6}$$

Where $F_{CD}$ *and* $l_w$ denote dimensionless fracture conductivity and fracture half-length (measured in ft) respectively; $h$ denotes reservoir thickness (in ft); $q$ denotes rate of production (in STB/day), $p_0$ and $p_{wf}$ denote initial pressure and flowing well pressure (in psi); $t$ denotes time (in hr); $\mu$, and $(C_t)_m$ denote viscosity (in cp) and total matrix compressibility (in $psi^{-1}$) respectively. Constants are conversion factors from SI units to customary field units.

## Simulation Results and Observations

### *Single fracture model*

Our simulation and interpretation of well-test signals in a NFR starts with a reservoir model containing a single natural fracture that intersects the well (Figure 7) as well as a single fracture located in the matrix at different distances to the well. Although such a model is unrealistic for a real reservoir condition, it allows us to apply analytical solutions (Bourdet 2002; Kuchuk & Biryukov 2015) and provide an important reference when interpreting pressure transient behaviour for complex cases.

These reference simulations show the well-studied flow regimes for different fracture conductivities and locations of the well with respect to the fracture. For example, low fracture conductivity (up to $F_{cD} = 100$) for a well intersecting fracture, the first flow regime observed in the pressure derivative is bilinear flow as shown on Figure 7(b). As fracture conductivity increases to $F_{cD} = 500$ (Figure 7b), the bilinear flow diminishes and linear flow emerges as the first flow regime before radial flow is attained (Gringarten *et al.* 1974, 1975; Cinco-Ley & Samaniego-V. 1981; Wong *et al.* 1986; Bourdet 2002). This is not the case for the same reservoir and fracture properties where the well is located in the matrix (Figure 6). It is well-understood that a well located near a single fracture first shows the effect of wellbore storage followed by radial flow in the matrix (depending on the distance on the nearby fracture) and then a minimum (dip) on the derivative reflecting the period of depletion from the fracture (Cinco-Ley *et al.* 1976; Abbaszadeh & Cinco-Ley 1995). Other simulation results of a well located in the matrix adjacent to fractures are presented later in Figure 10b, Figure 11b, Figure 12b, Figure 13b and Figure 14b.

In order to assess the validity and limitations of the Warren & Root (1963) dual-porosity model in the interpretation of NFR, we first simulate a number of models containing an idealised and regular

fracture network (Figure 10). We consider two different scenarios (Table 2, Model 4 and 5): A connected fracture model (Figure 10a) that consists of uniform rectangular parallelepipeds (20 m x 20 m x 1 m) of matrix blocks that are separated by two sets of perfectly orthogonal fractures. Secondly, we consider a disconnected fracture model (Figure 10b) that has the same properties as the connected model except that it contains only a single set of parallel fractures. In each of these models, we consider both, a well intersecting fracture(s) (Table 2, Model 4a and 5a) and a well located in the matrix (Table 2, Model 4b and 5b). In all cases, the well is located in the centre of the model or slightly offset from the centre (Figure 10), if the well is not intersecting a fracture. We consider fracture conductivities from 60md.m to $6x10^6$md.m, which yield dimensionless fracture conductivities of 0.1 to 10000. Table 2 contains further descriptions of the simulation models used here.

***Connected and disconnected fracture networks***

Figure 11 shows the resulting pressure derivatives for the connected fracture network. For the situation where a well intersects fractures (Figure 11a), the bilinear fracture flow regime (m = ¼) is observed at early time when the fracture conductivities are low ($F_{cD} = 0.1$ to 1). This regime then transitions through different periods until it reaches pseudo-radial flow when equilibrium between matrix and fracture flow is reached. However, surprisingly as fracture conductivity increases ($F_{cD} > 10$), the typical V-shape (or "dual-porosity dip") signature cannot be observed. The presence of well-connected fractures only produces a slanted S-shaped derivative profile shown by the solid line plots in Figure 11a.

**Figure 10**

**Figure 11**

In contrast, the typical V-shape can only be observed in models where the well is not intersecting any fractures (Figure 11b). Here, the pressure derivatives are characterised by two stabilisation periods where radial flow occurs that are separated by transition periods which cause troughs in the derivative plots. Initially, until the first period of radial flow (m = 0) commences, are the typical flow regimes of a homogeneous reservoir with the well located in the matrix. So until this period, the depletion is only from the matrix without contribution from the fractures. This is followed by a transition period (V-shape) where the contribution from the fractures becomes significant and the matrix and fracture pressure reach equilibrium. Once the two media equilibrate, the second pseudo-radial flow (m = 0) is observed. For the very low fracture conductivity ($F_{cD} < 1$), the dual-porosity behaviour is apparent via a broader, U-shaped, drop in the derivative. If $F_{cD} > 10$, the classical V-shape followed by a linear flow regime is observed before the derivatives increase rapidly as the stabilisation between the two systems is reached.

Figure 12a shows the simulated pressure derivatives for the disconnected fracture network. For the case where the well is intersecting a fracture (Figure 12a), fractures with low conductivity ($F_{cD} < 100$), lead to a pressure derivative that indicates clear bilinear flow, resulting in a slope of $m = 1/4$, before a period of pseudo-radial flow emerges. With an increase in fracture conductivity ($F_{cD} = 500$), a period of linear flow $m = 1/2$ is followed by a bilinear flow regime and eventually pseudo-radial flow. From the slope of the linear flow regime, the fracture half-length can be estimated. In these cases, none of the pressure transients show a dual-porosity signature. However, if the well does not intersect any fractures (Figure 12b), the dual-porosity behaviour is in many ways similar to the connected network shown in Figure 11b, independently of the fracture conductivity.

**Figure 12**

With the insights gained from the simple orthogonal fracture geometries discussed above, we simulated the pressure transient behaviour for the natural fracture patterns observed in the Jandaira

Formation (Figure 9). We identified locations with connected fracture (Figure 9 lower inset. See further description in Table 2, Model 6a and b) and disconnected fracture patterns (Figure 9 upper inset. See further description in Table 2, Model 7a and b) in the outcrop data and constructed models accordingly (Figures 13 and 14). This allowed us to compare the pressure transient behaviour observed for the idealised fracture pattern to the transient behaviour in more realistic fracture patterns. As in the simulations depicted in Figures 11 and 12, we ran simulations for wells intersecting a fracture and wells that are located in the matrix. Figures 13 and 14 show that the pressure transients for the realistic, outcrop-based fracture networks are similar to those in the idealised fracture systems. Again, the dual-porosity signature is only apparent if the well is located in the matrix, not intersecting a fracture (as shown by the dashed lines in Figure 13b and 14b).

**Figure 13**

**Figure 14**

***Effect of Fracture Skin***

A key observation is the counter-intuitive behaviour of the dual-porosity signal. It can only be observed if the well is located in the matrix, even in situations where the fractures are well connected. This is in contrast to the underlying theory of the Warren & Root (1963) dual-porosity model. Previous studies (*e.g.* Cinco-Ley & Samaniego 1977; Cinco-Ley *et al.* 1985; Gringarten 1987; Bourdet 2002; Kuchuk & Biryukov 2015) have discussed that the type of interporosity flow between the matrix and the fractures that is assumed in a computation, impacts the presence or absence of the dual-porosity signature, depending upon if the well is intersected by fractures or not. The above studies classified dual-porosity solutions into restricted interporosity flow and unrestricted interporosity flow. The restricted interporosity flow solution relates the dual-porosity behaviour to the presence of a skin at the fracture surface (Cinco-Ley & Samaniego 1977) and/or within fractures

(Cinco-Ley & Samaniego 1981), *i.e.*, damage caused by presence of minerals, filter cake, polymer-invaded zone etc., that restrict communications between the matrix and the fractures or within fractures. The presence of the interporosity skin causes the resulting pressure transient behaviour for a TIF model to show a dual-porosity V-shape similar to PSSIF (Valdes-Perez *et al.* 2011). The unrestricted interporosity flow is the same as the TIF model without taking any form of interporosity skin into account.

All the results presented so far in this paper relate to the unrestricted interporosity flow. This is because our model assumes simulation under TIF conditions and does not contain any interporosity skin that restrict flow within fractures or between matrix and fracture. No dual-porosity response is observed for a well intercepting fractures under TIF. To account for restricted interporosity flow (*i.e.*, TIF plus interporosity skin), we therefore have to modify the model and simulate for a well that is intersecting fractures with fracture damage (skin). The relationship between fracture skin and other reservoir properties is modelled after Cinco-Ley & Samaniego (1977), (see Figure 15) and defined as follows

$$s_f = \frac{\pi a_s}{2l_w}\left(\frac{k}{k_s} - 1\right), \tag{7}$$

where $s_f$, $a_s$ and $k_s$ denote fracture skin, width and permeability of skin zone respectively. Other parameters remain as previously defined. As before, we first explore the impact of fracture skin on the idealised connected and disconnected fracture networks before we proceed to model the more complex fracture geometries. The fracture skin was varied from 0 to 10 by assigning the corresponding value of the permeability of the skin zone

**Figure 15**

**Figure 16**

Figures 16 and 17 show the effect of fracture skin for the connected and disconnected fracture networks, respectively. A key observation is that higher positive fracture skin, *i.e.*, more fracture damage, leads to more obvious dual-porosity responses. This behaviour is particularly prominent for high fracture skin ($S \geq 5$) that locally restricts flow between fracture and matrix, although the permeability contrast between the fractures and matrix remains very low. It is clear that the dual-porosity signature is a result of the skin effect, *i.e.*, the restricted interporosity flow, rather than an effect of the well located in the fractures. Under this flow condition, the initial depletion from a fractured reservoir with skin emanates only from the fracture system; the discharge from the surrounding matrix is choked because of the reduction in permeability between the fractures and the matrix. This condition could allow flow from the fractures to stabilise and the transition period only follows after the flow from the matrix overcomes the barrier created by fracture skin.

Figure 17

***Effect of matrix permeability***

The fact that restricted interporosity flow can cause a clear dual-porosity signature raises the question if unrestricted interporosity flow could also show a dual-porosity signature if the matrix permeability is reduced. To test this, we keep the fracture permeability constant and successively reduce the matrix permeability, rather than changing $F_{cD}$ by keeping the matrix permeability constant and changing the fracture permeability. This still results in the same fracture permeability values, but there will be less flow in the matrix; this configuration is in agreement with one of the key assumption in the Warren & Root (1963) model, which only considers situations where flow within the matrix is negligibly small.

**Figure 18**

**Figure 19**

Figure 18 show the pressure transients for the idealised fracture networks with decreasing matrix permeability. In both, the connected network (Figure 18a) and disconnected network (Figure 18b), the dual-porosity signature becomes more prominent with decreasing matrix permeability. The reason for this response is similar to the restricted interporosity flow (Figure 16 and 17) in that the fluid exchange between fracture and matrix is reduced. However, since there is no fracture skin, the flow behaviour still falls into the category of unrestricted interporosity flow. There are two important observations. Firstly, the matrix permeability must be below 0.1 mD (Figure 18) for the dual-porosity signature to be clearly visible, *i.e.*, it is likely to occur more frequently in tight or unconventional reservoirs if there is no fracture damage. Secondly, the dual-porosity signature occurs at early time during our simulations and hence may not always be captured in the field data. Figure 19a and 19b show that even if the matrix block size increases from 20m (base case) to 160m; the dual-porosity V-shape is only visible within the first second of the well test. Larger matrix blocks (and increased fracture lengths) delay the onset of the dual-porosity signature relative to the base case because the fracture volume is increased and it takes slightly longer to deplete the fractures before the matrix recharge starts.

When applying the same changes in matrix permeability and matrix volume to the connected outcrop-based fracture patterns, (Figure 9 lower inset) and simulating a well intersecting fractures, the same pressure response in Figure 18a and Figure 19a is apparent in Figure 20a and 20b, respectively. Here, we rescaled the entire model dimensions and adjusted the fracture properties to ensure that the fracture aperture remains unchanged, *i.e.*, the increase in fracture volume is only due to the increased

623 fracture length, not fracture width.

624

625 **Figure 20**

626

627 ***Effect of fracture network connectivity and size***

628 We present another example where the dual-porosity signature can be observed for unrestricted
629 interporosity flow even if the matrix permeability is high. This scenario occurs if the well intersects a
630 fracture but this fracture belongs to a small fracture network or is an unconnected fracture that is
631 located in, but not connected to, larger fracture(s). In these cases, fluids are first produced from the
632 smaller fracture (network), then from the rock matrix, and then from the larger network. This implies
633 that the multi-scale nature that is common to many fracture networks (*e.g.* Odling 1997) can be
634 critical to the presence of the dual-porosity signature. To investigate this phenomenon quantitatively,
635 we run a number of test simulations for both, connected (Figure 21a insets) and disconnected fracture
636 (Figure 21b insets) networks and placed the well into an isolated fracture that is located close to, but
637 not connected to, the larger fracture system. The fracture geometries differ from those shown
638 previously in that they are even further idealised networks. Figure 21a and 21b show the resulting
639 pressure transients for the connected and disconnected network, respectively. In each case, we
640 observed that where the smaller fracture is not connected to the nearby large fracture(s), the first flow
641 regime is either bilinear or linear flow, depending on the fracture conductivity. In the examples
642 presented in these two figures with $F_{cD} = 1000$, the initial flow regime shows linear flow. Where the
643 fracture is not surrounded by any other fracture, this initial flow regime changes to pseudo-radial
644 flow, as illustrated in the single fracture case above (Figure 7). However, where our simulation
645 models contain other fractures surrounding the smaller ones that intersect the well, the resulting flow
646 behaviour is significantly different after the initial flow period (Figure 21a and 21b). Here, after the
647 smaller fractures are depleted, the larger fractures begin to deplete just as the transient response from
648 the small intersected fracture tends towards pseudo-radial flow with the surrounding matrix flow. This
649 second depletion of the larger, nearby fractures yields the dual-porosity V-shape observed here. After

650 this dual-porosity behaviour ceases, the entire system then stabilises. However, the moment the
651 smaller fracture is connected to any of the surrounding large fractures, the dual-behaviour signature
652 disappears because the entire fracture network responds as one single network.
653
654 **Figure 21**
655
656 **Figure 22**
657
658 The dependence of the dual-porosity signature on wells located in small-scale fractures that are
659 disconnected from the larger sale fractures is independent of the fracture geometries. Figures 22b and
660 23b show the pressure transients for the idealised connected fracture networks (Figures 22a. See
661 further description in Table 2, Model 8) and disconnected fracture networks (Figures 23a. See further
662 description in Table 2, Model 9). In the disconnected fracture network, smaller disconnected fractures
663 have been added but are kept separated from the closest large fracture by distances of 5, 2, and 1m,
664 respectively. Importantly, the orientation of the minor fractures does not impact the presence or
665 absence of the dual-porosity signature; only the distance of separation between the fractures is
666 important. As noted above, the fracture half-length can be estimated from the linear flow regime. Here
667 we estimate the fracture half length of the small fracture from the early linear flow regime. When the
668 small fracture is connected to the nearby large fractures, the flow behaviour is different. Figure 22b
669 shows that small connected fracture profile is an S-shape, consistent with our results for connected
670 fracture network presented in Figure 11a. In the disconnected fracture network (Figure 23b), the
671 minor connected fracture results in a linear flow regime which then transitions to pseudo-radial flow,
672 as already observed in the findings shown in Figure 12a. The half-length estimated from the linear
673 flow regime in the disconnected fracture network corresponds to that of the combined lengths of the
674 small and large fractures. This is in contrast to the situation where the small fracture is isolated and
675 only the length of the small fracture can be estimated. Results presented in Figure 21 to 23 confirm

676 that a fractured reservoir with unrestricted interporosity flow generates a dual-porosity signature if the
677 well is intersecting a smaller fracture located close to a large fracture or fracture network.

678

679 **Figure 23**

680

681 However, not all small fractures that are disconnected from the larger fractures cause a clear dual-
682 porosity behaviour (*i.e.*, the V-shape profile of Warren & Root). To quantify when the small,
683 disconnected fractures cause a dual-porosity signature, we establish a simple relationship, the
684 effective length ratio $ELR$, between the lengths of the small and large fracture(s). We define ELR as

$$ELR = \frac{l_{suf}}{L_{lf}}, \tag{8}$$

685 where $l_{suf}$ and $L_{lf}$ denotes length of the small unconnected fracture and length of nearby large
686 fracture respectively

687

688 **Figure 24**

689

690 **Figure 25:**

691

692 Using this relationship, we run simulations on the idealised disconnected fracture networks, adding
693 fractures with $ELR$ ranging from 0.1 to 1.0 (Figure 24a. See further description in Table 2, Model 10).
694 The resulting pressure transients (Figure 24b) show that the dual-porosity signature is more prominent
695 when the length of the smaller fracture is small compared to the nearby larger fracture. As the value of
696 $ELR$ increases, the dual-porosity signature diminishes. Once $ELR$ exceeds 0.5, the dual-porosity
697 signature is absent. Furthermore, it can be observed from Figure 24(b) that the symmetry of the limbs
698 of the dual-porosity "dip" is also a function of the $ELR$. Small values of $ELR$ tend to yield a "V-

shape" curve with first limbs (upper left to bottom right direction) that are more symmetrical to the second limbs (bottom left to upper right direction) while large ELR values produce first limbs that are asymmetrical to the other limb. Flow regimes identified prior to the emergence of this first limb depend on the properties of the smaller fracture intersected by the well. The second limb of this shape relates to fracture conductivity and nature of fracture network connectivity.

The impact of $ELR$ on the dual-porosity behaviour is also apparent in the outcrop-based fracture patterns (shown in Figure 9 lower inset). We identified unconnected smaller fractures with different lengths (Figure 25a), calculated the corresponding $ELR$, and simulate the pressure transients (Figure 25b) for cases where the well intersects these smaller fractures. The results show a clear dual-porosity signature for all cases except for case F5 where $ELR = 0.56$, *i.e.*, above the cut-off value of 0.5

## Conclusions

We applied a geoengineering workflow with the discrete fracture matrix modelling (DFM) technique and unstructured-grid reservoir simulator to generate synthetic pressure transient responses for idealised fractures and realistic fracture networks. We demonstrated when dual-porosity models are valid and systematically present alternative interpretations to reservoir features that characterise this behaviour in naturally fractured reservoirs. Furthermore, we quantify when and why the assumptions breakdown when interpreting well test data from naturally fractured reservoirs.

Based on the numerical simulations and the results presented, we arrived at the following conclusions:

1. For a well intersecting a fracture, the dual-porosity "dip" of Warren & Root (1963) well testing signature is observed in Type II and III Nelson's (2001) classification due to the following situations
    a. The effect of fracture skin;
    b. The matrix permeability is very tight (less than 1mD), similar to unconventional reservoirs (*e.g.* tight gas sands);

c. The well intersects a small unconnected fracture located near a single large fracture or a large fracture network;

2. Reservoirs can be fractured even if the dual-porosity “V-shape” in the well test data is absent.

Natural fractures have a significant effect on hydrocarbon recovery and reservoir productivity. Therefore, it critical to identify fractures and assess the flow behaviour early on during a development to improve reservoir performance and optimise recovery. A reservoir characterisation which relies upon the appearance of a dual-porosity V-shape on pressure derivatives reduces the chance of identifying and properly interpreting fractures from well-tests data. If not properly characterised (or missed), fractures could cause production issues and results to detrimental effect on hydrocarbon recovery, including early water and gas breakthrough. Our results show a range of flow behaviour from a pressure transient analysis that could indicate the presence of fractures in a reservoir where the classic dual-porosity V-shape is absent.

On the other hand, where the conventional dual-porosity signature is recognisable, we provided insights into the key geological features (including fracture skin, matrix permeability, fracture network connectivity and size) that characterise this response. Our findings on wells intersecting smaller fractures give insight on the occurrence of fracture network sizes and their connectivity in a field. Identification and quantification of multiscale fractures is invaluable in assessing the role of different fracture sets during production. The influence of these fractures can be harnessed when planning IOR/EOR schemes to improve recovery.

We observed that the limbs of the dual-porosity “dip” can provide further diagnosis about the fracture network conductivity and connectivity. Generally, a shallow symmetrical “dip” indicates low fracture conductivities and a steep “dip” points to high fracture conductivities. For the high fracture conductivity cases, the second limb of the “V-shape” can differentiate a connected fracture network (with ½ slope) from a disconnected fracture network (with ¼ slope). Where the dual-porosity “dip”

results from the well intersecting a small-unconnected fracture located near a large fracture or fracture network, the symmetry of the first limb to the second is a function of the small fracture.

## Acknowledgements

The authors are thankful to PTDF for funding David's PhD and Foundation CMG for supporting Sebastian's Chair for Carbonate Reservoir Simulation. We further thank CMG Ltd for access to IMEX, Weatherford for access to Pansystem, and SINTEF for access to MRST and their support with MRST.

## References

Abbaszadeh, M., & Cinco-Ley, H. (1995). Pressure-transient behavior in a reservoir with a finite-conductivity fault. *SPE Formation Evaluation*, *10*(1), 26–32. http://doi.org/10.2118/24704-PA.

Agada, S., Chen, F., Geiger, S., Toigulova, G., Agar, S., Shekhar, R., Immenhauser, A. (2014). Numerical simulation of fluid-flow processes in a 3D high-resolution carbonate reservoir analogue. *Petroleum Geoscience*, *20*(1), 125–142. http://doi.org/10.1144/petgeo2012-096.

Agar, S. M., Geiger, S., & Matthäi, S. K. (2010). The Impact of Hierarchical Fracture Networks on Flow Partitioning in Carbonate Reservoirs : Examples Based on a Jurassic Carbonate Ramp Analog from the High Atlas , Morocco. *SPE Annual Technical Conference and Exhibition*, *2*, 1–19. http://doi.org/10.2118/135135-MS.

Ahmadov, R., Aydin, A., Karimi-Fard, M., & Durlofsky, L. J. (2007). Permeability upscaling of fault zones in the Aztec Sandstone, Valley of Fire State Park, Nevada, with a focus on slip surfaces and slip bands. *Hydrogeology Journal*, *15*(7), 1239–1250. http://doi.org/10.1007/s10040-007-0180-2.

Aljuboori, F., Bisdom, K., Corbett, P.W.M., Bertotti, G. and Geiger, S. (2015). Using outcrop data for geological well test modelling in fractured reservoirs, 77th EAGE Conference & Exhibition, Maldrid, Spain, 1–4 June 2015.

Bahrainian, S. S., Dezfuli, A. D., & Noghrehabadi, A. (2015). Unstructured grid generation in porous domains for flow simulations with discrete-fracture network model. *Transport in Porous Media*, *109*(3), 693–709. http://doi.org/10.1007/s11242-015-0544-3.

Barenblatt, G. ., Zheltov, I. ., & Kochina, I. (1960). Basic concepts in the theory of seepage of homogeneous liquids in fissured rocks [strata]. *Journal of Applied Mathematics and Mechanics*, *24*(5), 1286–1303. http://doi.org/10.1016/0021-8928(60)90107-6.

Belayneh, M., Geiger, S., & Matthäi, S. K. (2006). Numerical simulation of water injection into layered fractured carbonate reservoir analogs. *AAPG Bulletin*, *90*(10), 1473–1493. http://doi.org/10.1306/05090605153.

Belayneh, M., Matthai, S. ., & Cosgrove, J. . (2007). The implications of fracture swarms in the Chalk of SE England on the tectonic history of the basin and their impact on fluid flow in high-porosity, low-permeability rocks. *Geological Society, London, Special Publications*, *272*, 499–517. http://doi.org/10.1144/GSL.SP.2007.272.01.25.

Belayneh, M. W., Matthai, S. K., Blunt, M. J., & Rogers, S. F. (2009). Comparison of deterministic with stochastic fracture models in water-flooding numerical simulations. *AAPG Bulletin*, *93*(11), 1633–1648. http://doi.org/10.1306/07220909031.

Beliveau, D., Payne, D., & Mundry, M. (1993). Waterflood and CO2 Flood of the Fractured Midale Field (includes associated paper 22947 ). *Journal of Petroleum Technology*, *45*(9), 881–887. http://doi.org/10.2118/22946-PA.

Bertotti, G., Bisdom, K., van Eijk, M., Hameka, F., Vis, A., Bezerra, H., & Reijmer, J. (2014). Fractures and fracture networks in carbonate reservoirs: A geological perspective, in *AAPG International Conference & Exhibition, 14-17 September 2014*. Istanbul, Turkey.

Bertotti, G., de Graaf, S., Bisdom, K., Oskam, B., Vonhof, H., Bezerra, F. H., Reijmer, J. and Cazarin, C. (2017), Fracturing and fluid flow during post-rift subsidence in carbonate of the Jandaíra Formation, Potiguar Basin, NE Brazil. Basin Research, p. 1–18, doi:10.1111/bre.12246.

Berumen, S., Tiab, D., & Rodriguez, F. (2000). Constant rate solutions for a fractured well with an asymmetric fracture. *Journal of Petroleum Science and Engineering*, *25*(1), 49–58. http://doi.org/10.1016/S0920-4105(99)00053-4.

Bisdom, K., G. Bertotti, and F. H. Bezerra, 2017, Inter-well scale natural fracture geometry and permeability variations in low-deformation carbonate rocks: Journal of Structural Geology, v. 97, p. 23–36, doi:10.1016/j.jsg.2017.02.011.

Bisdom, K., Bertotti, G., & Nick, H. M. (2016). The impact of different aperture distribution models and critical stress criteria on equivalent permeability in fractured rocks. *Journal of Geophysical Research: Solid Earth*, *119*, 8132–8153. http://doi.org/10.1002/2015JB012657.

Bisdom, K., H. M. Nick, and G. Bertotti, 2017, An integrated workflow for stress and flow modelling using outcrop-derived discrete fracture networks: Computers & Geosciences, v. 103, p. 21–35, doi:10.1016/j.cageo.2017.02.019.

Bogdanov, I. I., Mourzenko, V. V., Thovert, J.-F. and Adler, P. M. (2003) 'Pressure drawdown well tests in fractured porous media', Water Resources Research, 39(1). doi: 10.1029/2000WR000080.

Boulton, N. S., & Streltsova, T. D. (1977). Unsteady flow to a pumped well in a fissured water-bearing formation. *Journal of Hydrology*, *35*(3), 257–270.

Bourbiaux, B. (2010). Fractured Reservoir Simulation: a Challenging and Rewarding Issue. *Oil & Gas Science and Technology – Revue de l'Institut Français Du Pétrole*, *65*(2), 227–238. http://doi.org/10.2516/ogst/2009063.

Bourdet, D. (2002). *Well Test Analysis: the Use of Advanced Interpretation Models Handbook of Petroleum Exploration and Production Vol 3* (First). Elsevier.

Bourdet, D., Ayoub, J. A., & Pirard, Y. M. (1989). Use of pressure derivative in well test interpretation. *SPE Formation Evaluation*, *4*(2), 293–302. http://doi.org/10.2118/12777-PA.

Bourdet, D., Ayoub, J., & Kniazeff, V. (1983). Interpreting well tests in fractured reservoirs. *World Oil;(United States)*, *197*(5).

Bourdet, D., & Gringarten, A. C. (1980). Determination of fissure volume and block size in fractured reservoirs by type-curve analysis. In *SPE Annual Technical Conference and Exhibition, 21-24 September 1980, Dallas, Texas*. http://doi.org/10.2118/9293-MS.

Bourdet, D., Whittle, T. M., Douglas, A. A., & Pirard, Y. M. (1983). A new set of type cuves simplifies well test analysis. *World Oil*, *196*(6), 95–106. http://doi.org/10.2118/16812-PA.

Branets, L. V., Ghai, S. S., Lyons, S. L. L., & Wu, X.-H. (2009). Challenges and technologies in reservoir modeling. *Communications in Computational Physics*, *6*(1), 1–23. http://doi.org/10.4208/cicp.2009.v6.p1.

Chen, Z.-X. (1989). Transient flow of slightly compressible fluids through double porosity, double-permeability systems - a state-of-the-art review. *Transport in Porous Media*, *4*(2), 147–184.

Cinco-Ley, H. (1996). Well-testing analysis for naturally fractured reservoirs. *Journal of Petroleum Technology*, *48*(1), 51–54.

Cinco-Ley, H., & Samaniego, V. F. (1977). Effect of wellbore storage and damage on the transient pressure behavior of vertically fractured wells. In *SPE Annual Fall Technical Conference and Exhibition, 9-12th Oct 1977*.

Cinco-Ley, H., & Samaniego, V. F. (1982). Pressure transient analysis for naturally fractured reservoirs. In *SPE Annual Technical Conference and Exhibition, 26-29 Sept. 1982*. http://doi.org/10.2118/11026-MS.

Cinco-Ley, H., Samaniego, V. F., & Kucuk, F. (1985). The pressure transient behavior for naturally fractured reservoirs with multiple block size. In *SPE Annual Technical Conference and Exhibition, 22-25 September 1985*.

Cinco-Ley, H., Samaniego V., F., & Dominguez A., N. (1976). Unsteady-state flow behavior for a well near a natural fracture. In *SPE Annual Fall Technical Conference and Exhibition, 3-6 Oct. 1976*.

Cinco-Ley, H., & Samaniego-V., F. (1981). Transient pressure analysis for fractured wells. *Journal of Petroleum Technology*, *33*(9), 1749–1766. http://doi.org/10.2118/7490-PA.

Corbett, P. W. M., Geiger, S., Borges, L., Garayev, M., & Valdez, C. (2012). "The third porosity system: understanding the role of hidden pore systems in well-test interpretation in carbonates." *Petroleum Geoscience*, *18*(1), 73–81. http://doi.org/10.1144/1354-079311-010.

de Graaf, S., J. J. G. Reijmer, G. V. Bertotti, F. H. R. Bezerra, C. L. Cazarin, K. Bisdom, and H. B. Vonhof, 2017, Fracturing and calcite cementation controlling fluid flow in the shallow-water carbonates of the Jandaíra Formation, Brazil: Marine and Petroleum Geology, v. 80, p. 382–393, doi:10.1016/j.marpetgeo.2016.12.014.

de Swaan O., A. (1976). Analytic solutions for determining naturally fractured reservoir properties by well testing. *Society of Petroleum Engineers Journal*, *16*(3), 117–122. http://doi.org/10.2118/5346-PA.

Earlougher, R. C. J. (1977). Advances in well test analysis. *Society of Petroleum Engineers of AIME, Dallas, Monograph*, 264.

Edery, Y., Porta, G. M., Guadagnini, A., Scher, H., & Berkowitz, B. (2016). Characterization of Bimolecular Reactive Transport in Heterogeneous Porous Media. *Transport in Porous Media*, *115*(2), 291–310. http://doi.org/10.1007/s11242-016-0684-0.

Egya, D., Geiger, S., Corbett, P., March, R., Bisdom, K., Bertotti, G., & Bezerra, H. (2016). Assessing the validity and limitations of dual-porosity models using geological well testing for fractured formations. In *78th EAGE Conference & Exhibition 2016, Vienna, Austria.*

Egya, D., Geiger, S., Corbett, P., March, R. (2017). The effect of fracture skin, network connectivity, and network size on well-test responses in naturally fractured reservoirs. In *79th EAGE Conference & Exhibition 2017, Paris, France.*

Fernø, M. (2012). Enhanced Oil Recovery in Fractured Reservoirs. *Introduction to Enhanced Oil Recovery (EOR) Processes and Bioremediation of Oil -Contaminated Sites*, 89–110. Retrieved from http://cdn.intechopen.com/pdfs/37039.

Firoozabadi, A. (2000). Recovery mechanisms in fractured reservoirs and field performance. *Journal of Canadian Petroleum Technology*, *39*(11), 13–17. http://doi.org/10.2118/00-11-DAS.

Geiger, S., Dentz, M., & Neuweiler, I. (2013). A novel multi-rate dual-porosity model for improved simulation of fractured and multiporosity reservoirs. *SPE Journal*, *18*(4), 670–684. http://doi.org/10.2118/148130-MS.

Geiger, S., & Emmanuel, S. (2010). Non-Fourier thermal transport in fractured geological media. *Water Resources Research*, *46*(7), 1–13. http://doi.org/10.1029/2009WR008671.

Geiger, S., & Matthäi, S. (2014). What can we learn from high-resolution numerical simulations of single- and multi-phase fluid flow in fractured outcrop analogues? *Geological Society, London, Special Publications*, *374*(1), 125–144. http://doi.org/10.1144/SP374.8.

Geiger, S., Matthäi, S., Niessner, J., & Helmig, R. (2009). Black-oil simulations for three-component,

three-phase flow in fractured porous media. *SPE Journal*, *14*(2), 338–354. http://doi.org/10.2118/107485-PA.

Gilman, J. R., & Kazemi, H. (1983). Improvements in Simulation of Naturally Fractured Reservoirs. *Society of Petroleum Engineers Journal*, *23*(4), 695–707. http://doi.org/10.2118/10511-PA

Gringarten, A. C. (1984). Interpretation of tests in fissured and multilayered reservoirs with double porosity behavior: theory and practice. *Journal of Petroleum Technology*, *36*(4), 549–564.

Gringarten, A. C. (1987). How to recognize "double-porosity" systems from well tests. *Journal of Petroleum Technology*, *39*(6), 631–633. http://doi.org/10.2118/16437-PA.

Gringarten, A. C., Ramey, H. J., & Raghavan, R. (1974). Unsteady-state pressure distributions created by a well with a single infinite-conductivity vertical fracture. *Society of Petroleum Engineers Journal*, *14*(4), 347–360.

Gringarten, A. C., Ramey Jr, H. J. ., & Raghavan, R. (1975). Applied pressure analysis for fractured wells. *Journal of Petroleum Technology*, *27*(7), 887–892. http://doi.org/10.2118/5496-PA.

Hardebol, N. J., Maier, C., Nick, H., Geiger, S., Bertotti, G., & Boro, H. (2015). Multiscale fracture network characterisation and impact on flow. *Journal of Geophysical Research : Solid Earth*, 767–787. http://doi.org/10.1002/2015JB012352.Received.

Howell, J. A., Martinius, A. W., Good, T. R., Howell, J. A., Martinius, A. W., & Good, T. R. (2014). The application of outcrop analogues in geological modelling : a review , present status and future outlook. In A. W. Martinius, J. A. Howell, & T. R. Good (Eds.), *Sediment-Body Geometry and Heterogeneity: Analogue Studies for Modelling the Subsurface* (pp. 1–25). Geological Society, London, Special Publications, 387. http://doi.org/10.1144/SP387.12.

Hyman, J. D., Gable, C. W., Painter, S. L., & Makedonska, N. (2014). Conforming delaunay triangulation of stochastically generated three dimensional discrete fracture networks : a feature rejection algorithm for meshing strategy. *SIAM J. SCI. COMPUT.*, *36*(4), 1871–1894.

KAPPA. (2012). KAPPA *Dynamic Data Analysis (DDA) - v4.12.03*.

Karimi-Fard, M., Durlofsky, L. J. and Aziz, K. (2004) 'An efficient discrete-fracture model applicable for general-purpose reservoir simulators', SPE Journal, 9(2), pp. 227–236. doi: 10.2118/88812-PA.

Kazemi, H. (1969). Pressure transient analysis of naturally fractured reservoirs with uniform fracture distribution. *Society of Petroleum Engineers Journal*, *9*(4), 451–462. http://doi.org/10.2118/2156-A.

Kazemi, H., Seth, M. S., & Thomas, G. W. (1969). The interpretation of interference tests in naturally fractured reservoirs with uniform fracture distribution. *Society of Petroleum Engineers Journal*, *9*(4), 463–472. http://doi.org/10.2118/2156-PA.

Kim, J.-G. and Deo, M. D. (2000) 'Finite element, discrete-fracture model for multiphase flow in porous media', AlChE Journal, 46(6), pp. 1120–1130. doi: 10.1002/aic.690460604.

Kuchuk, F., & Biryukov, D. (2014). Pressure-transient behavior of continuously and discretely fractured reservoirs. *SPE Reservoir Evaluation & Engineering*, *17*(1), 82–97. http://doi.org/10.2118/158096-PA.

Kuchuk, F., & Biryukov, D. (2015). Pressure-transient tests and flow regimes in fractured reservoirs. *SPE Reservoir Evaluation and Engineering*, *18*(2), 187–204.

Kuchuk, F., Biryukov, D., & Fitzpatrick, T. (2015). Fractured-reservoir modeling and interpretation. *SPE Journal*, *20*(5), 983–1,004.

Lemonnier, P., & Bourbiaux, B. (2010a). Simulation of naturally fractured reservoirs. state of the art - part 1 - physical mechanisms and simulator formulation. *Oil & Gas Science and Technology – Revue de l'Institut Français Du Pétrole*, *65*(2), 239–262. http://doi.org/10.2516/ogst/2009066

Lemonnier, P., & Bourbiaux, B. (2010b). Simulation of naturally fractured reservoirs. state of the art - part 2 - matrix-fracture transfers and typical features of numerical studies. *Oil & Gas Science and Technology – Revue de l'Institut Français Du Pétrole*, *65*(2), 263–286. http://doi.org/10.2516/ogst/2009067.

Lie, K.-A., Krogstad, I. S., Natvig, J. R., Nilsen, H. M., & Skaflestad, B. (2012). Open-source MATLAB implementation of consistent discretisations on complex grids. Comput. Geosci., Vol. 16, No. 2, pp. 297-322.

Mallison, B. T., Hui, M. H., & Narr, W. (2010). Practical gridding algorithms for discrete fracture modeling workflows. In *ECMOR XII, 12th European Conference on the Mathematics of Oil Recovery, 6-9 September 2010, Oxford, UK* (pp. 1–11). http://doi.org/A032.

946 Matthäi, S. K., & Belayneh, M. (2004). Fluid flow partitioning between fractures and a permeable
947 rock matrix. *Geophysical Research Letters*, *31*(2), 1–5. http://doi.org/10.1029/2003GL019027.
948 Matthäi, S. K., & Roberts, S. G. (1996). The influence of fault permeability on single-phase fluid flow
949 near fault-sand intersections: Results from steady-state high-resolution models of pressure-
950 driven fluid flow. *AAPG Bulletin*, *80*(11), 1763–1779. http://doi.org/10.1306/64EDA15E-1724-
951 11D7-8645000102C1865D.
952 Mavor, M. J., & Cinco-Ley, H. (1979). Transient pressure behavior of naturally fractured reservoirs.
953 In *SPE California Regional Meeting, 18-20 April 1979*.
954 Moench, A. F. (1984). Double-porosity models for a fissured groundwater reservoir with fracture
955 skin. *Water Resources Research*, *20*(7), 831–846.
956 Morton, K. L., Booth, R. J. S., Chugunov, N., Biryukov, D., Fitzpatrick, A. F., & Kuchuk, F. J.
957 (2013). Global sensitivity analysis for natural fracture geological modeling parameters from
958 pressure transient tests,. In *EAGE Annual Conference & Exhibition incorporating SPE Europec*
959 *held in London, United Kingdom, 10–13 June 2013*.
960 Morton, K. L., Kuchuk, F. J., & Fitzpatrick, A. J. (2015). Active and Interference Well Pressure
961 Transient Data Interpretation in Naturally Fractured Reservoirs. In *77th EAGE Conference and*
962 *Exhibition 1-4 June 2015*.
963 Morton, K. L., Nogueira, P. de B., Booth, R. J. S., & Kuchuk, F. J. (2012). Integrated interpretation
964 for pressure transient tests in discretely fractured reservoirs. In *EAGE Conference & Exhibition*
965 *incorporating SPE EUROPEC 2012 Copenhagen, Denmark, 4-7 June 2012*.
966 Møyner, O., & Lie, K.-A. (2016). A multiscale restriction-smoothed basis method for high contrast
967 porous media represented on unstructured grids. *Journal of Computational Physics*, *304*, 46–71.
968 http://doi.org/10.1016/j.jcp.2015.10.010.
969 Najurieta, H. L. (1980). A theory for pressure transient analysis in naturally fractured reservoirs.
970 *Journal of Petroleum Technology*, *32*(7), 1–241.
971 Narr, W., Schechter, D. W., & Thompson, L. B. (2006). *Naturally fractured reservoir*
972 *characterization*. Richardson, TX: Society of Petroleum Engineers.
973 Nelson, R. A. (2001). *Geologic analysis of naturally fractured reservoirs*. Gulf Professional

Publishing.

Odeh, A. S. (1965). Unsteady-state behavior of naturally fractured reservoirs. *Society of Petroleum Engineers Journal*, *5*(1), 60–66. http://doi.org/10.2118/966-PA.

Odling, N. E. (1997). Scaling and connectivity of joint systems in sandstones from western Norway. *Journal of Structural Geology*, *19*(10), 1257–1271. http://doi.org/10.1016/S0191-8141(97)00041-2.

Olorode, O. M., Freeman, C. M., Moridis, G. J., & Blasingame, T. A. (2013). High-resolution numerical modeling of complex and irregular fracture patterns in shale-gas reservoirs and tight gas reservoirs. *SPE Reservoir Evaluation & Engineering*, *16*(4), 443–455.

Ramsey, J. M., and F. M. Chester, 2004, Hybrid fracture and the transition from extension fracture to shear fracture.: Nature, v. 428, no. 6978, p. 63–6, doi:10.1038/nature02333.

Seers, T. D., & Hodgetts, D. (2013). Comparison of digital outcrop and conventional data collection approaches for the characterization of naturally fractured reservoir analogues. In G. H. Spence, J. Redfern, R. Aguilera, T. G. Bevan, J. W. Cosgrove, G. D. Couples, & J.-M. Daniel (Eds.), *Advances in the study of fractured reservoirs* (Vol. 374, pp. 51–77). Geological Society, London, Special Publications, 374. http://doi.org/10.1144/SP374.13.

Serra, K., Reynolds, A. ., & Raghavan, R. (1983). New Pressure Transient Analysis Methods for Naturally Fractured Reservoirs. *Journal of Petroleum Technology*, *35*(12), 2271–2283. http://doi.org/10.2118/10780-PA.

Shewchuck, J. R. (2002). Delaunay refinement algorithms for triangular mesh generation. *Applied Computational Geometry*, *22*(1), 21–74. http://doi.org/doi:10.1016/S0925-7721(01)00047-5

Spence, G. H., Couples, G. D., Bevan, T. G., Aguilera, R., Cosgrove, J. W., Daniel, J.-M., & Redfern, J. (2014). Advances in the study of naturally fractured hydrocarbon reservoirs: a broad integrated interdisciplinary applied topic. In G. H. Spence, G. D. Couples, T. G. Bevan, R. Aguilera, J. W. Cosgrove, J.-M. Daniel, & J. Redfern (Eds.), *Advances in the study of fractured reservoirs* (Vol. 374, pp. 1–22). Geological Society, London, Special Publications. http://doi.org/10.1144/SP374.19.

Streltsova, T. D. (1976). Hydrodynamics of groundwater flow in a fractured formation. *Water*

*Resources Research*, *12*(3), 405–414. http://doi.org/10.1029/WR012i003p00405.

Streltsova, T. D. (1983). Well pressure behavior of a naturally fractured reservoir. *Society of Petroleum Engineers Journal*, *23*(5), 769–780.

Sun, J., & Schechter, D. (2015). Optimization-based unstructured meshing algorithms for simulation of hydraulically and naturally fractured reservoirs with variable distribution of fracture aperture, spacing, length and strike. *SPE Reservoir Evaluation & Engineering*, *18*(4), 463–480.

Sun, J., Schechter, D., Texas, A., & Huang, C. (2015). Sensitivity analysis of unstructured meshing parameters on production forecast of hydraulically fractured horizontal wells. In *Abu Dhabi International Petroleum Exhibition and Conference, 9-12 November 2015*. Society of Petroleum Engineers. http://doi.org/10.2118/177480-MS.

Syihab, Z. (2009). *Simulation of discrete fracture netmowrk using flexible voronoi gridding (Doctoral dissertation)*. Texas A&M University.

Valdes-perez, A. R., Pulido, H., Cinco-Ley, H. and Galicia-muñoz, G. (2011) 'a new bilinear flow model for naturally fractured reservoirs with transient interporosity transfer', in proceedings, Thirty-Sixth Workshop on Geothermal Reservoir Engineering Stanford University, Stanford, California, January 31 - February 2, 2011.

Wanjing, L., & Changfu, T. (2014). Pressure-transient analysis of multiwing fractures connected to a vertical wellbore. *SPE Journal*, *20*(2), 360–367.

Warren, J. E., & Root, P. J. (1963). The behavior of naturally fractured reservoirs. *Society of Petroleum Engineers Journal*, *3*(3), 245–255.

Wei, L., Hadwin, J., Chaput, E., Rawnsley, K., & Swaby, P. (1998). Discriminating fracture patterns in fractured reservoirs by pressure transient tests. In *SPE Annual Technical Conference and Exhibition, New Orleans, Lousiana, U.S.A., 27-30 September 1998, SPE 49233*.

Wilson, C. E., Aydin, A., Karimi-Fard, M., Durlofsky, L. J., Sagy, A., Brodsky, E. E., … Kellogg, L. H. (2011). From outcrop to flow simulation: Constructing discrete fracture models from a LIDAR survey. *AAPG Bulletin*, *95*(11), 1883–1906. http://doi.org/10.1306/03241108148.

Wong, D. W., Harrington, A. G., & Cinco-Ley, H. (1986). Application of the pressure derivative function in the pressure transient testing of fractured wells. *SPE Formation Evaluation*, *1*(5),

470–480. http://doi.org/10.2118/13056-PA.

Zheng, S. Y., Legrand, V. M., & Corbett, P. W. M. (2007). Geological model evaluation through well test simulation : a case study from the Wytch farm oilfield , southern England. *Journal of Petroleum Geology*, *30*(1), 41–58.

Zhou, F., Shi, A., & Wang, X. (2014). An efficient finite difference model for multiphase flow in fractured reservoirs. *Petroleum Exploration and Development*, *41*(2), 262–266. http://doi.org/10.1016/S1876-3804(14)60031-8.

**Tables**

| | |
|---|---|
| Reservoir initial pressure, $p_0$ (psi) | 4351 |
| Flow rate, q (bbl/day) | 31.45 |
| Matrix porosity, $\varphi_m$ (fraction) | 0.3 |
| Matrix permeability, $k_m$ (md) | 10 |
| Fracture porosity, $\varphi_f$ (fraction) | 1.0 |
| Oil viscosity, $\mu_o$ (cp) | 1.0 |
| Oil density, $\rho_o$ ($kg/m^3$) | 700 |
| Oil formation volume factor, rb/stb | 1.0 |
| Total compressibility ($psi^{-1}$) | $6.8948 \times 10^{-6}$ |

***Table 1:*** *Reservoir model and fluid properties*

1044

| **Model name** | **Well location** | **Model description and dimension** |
|---|---|---|
| Model 1: Unfractured (matrix) model | matrix | 200m x 200m x 1m homogeneous matrix model used for validation and sensitivities study |
| Model 2: Single fracture model | fracture | 200m x 200m x 1m homogeneous matrix model with two-wing (single) fracture used for validation. $F_{cD}$ 1 : 500 |
| Model 3: Multiple intersection (multiwings) fracture model | fracture | 200m x 200m x 1m homogeneous matrix model with six-wing (multiple) fractures and asymmetric factors used for validation. $F_{cD}$ of 10 |
| Model 4a: Idealised connected fractures network | fracture | 4km x 4km x 1m homogeneous matrix model with idealised connected fracture network. $F_{cD}$ of 0.1 to 10000 |
| Model 4b: Idealised connected fractures network | matrix | 4km x 4km x 1m homogeneous matrix model with idealised connected fracture network. $F_{cD}$ of 0.1 to 10000 |
| Model 5a: Idealised disconnected fractures network | fracture | 4km x 4km x 1m homogeneous matrix model with idealised disconnected fracture network. $F_{cD}$ of 0.1 to 1000 |
| Model 5b: Idealised disconnected fractures | matrix | 4km x 4km x 1m homogeneous matrix model with idealised disconnected fracture |

| | | |
|---|---|---|
| network | | network. $F_{cD}$ of 0.1 to 1000 |
| Model 6a: Outcrop example of connected fractures network | fracture | 550m x 550m x 1m homogeneous matrix subset-model with realistic outcrop connected fracture patterns. $F_{cD}$ of 0.1 to 10 |
| Model 6b: Outcrop example of connected fractures network | matrix | 550m x 550m x 1m homogeneous matrix subset-model with realistic outcrop connected fracture patterns. $F_{cD}$ of 0.1 to 10 |
| Model 7a: Outcrop example of disconnected fractures network | fracture | 480m x 450m x 1m homogeneous matrix subset-model with realistic outcrop disconnected fracture patterns. $F_{cD}$ of 0.1 to 10 |
| Model 7b: Outcrop example of disconnected fractures network | matrix | 480m x 450m x 1m homogeneous matrix subset-model with realistic outcrop disconnected fracture patterns. $F_{cD}$ of 0.1 to 10 |
| Model 8: Idealised connected fractures network with small fractures | fracture | 4km x 4km x 1m homogeneous matrix model with idealised connected fracture network and (un)connected small fractures. $F_{cD}$ of 1000 |
| Model 9: Idealised disconnected fractures network with small fractures | fracture | 4km x 4km x 1m homogeneous matrix model with idealised disconnected fracture network and (un)connected small fractures. $F_{cD}$ of 1000 |
| Model 10: Idealised disconnected fractures | fracture | 4km x 4km x 1m homogeneous matrix model with idealised disconnected fracture |

| | | |
|---|---|---|
| network with increasing small fracture | | network and different lengths of unconnected small fracture. $F_{cD}$ of 1000 |

***Table 2:*** *Summary of simulation models with grid dimensions and well locations*

1045

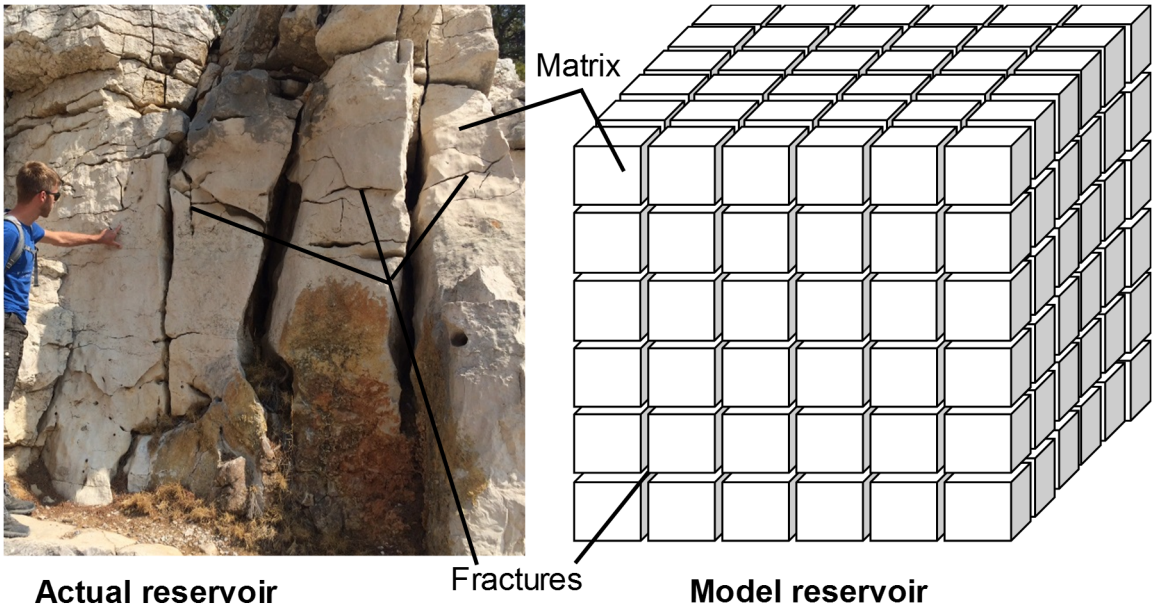


**Figure 1**

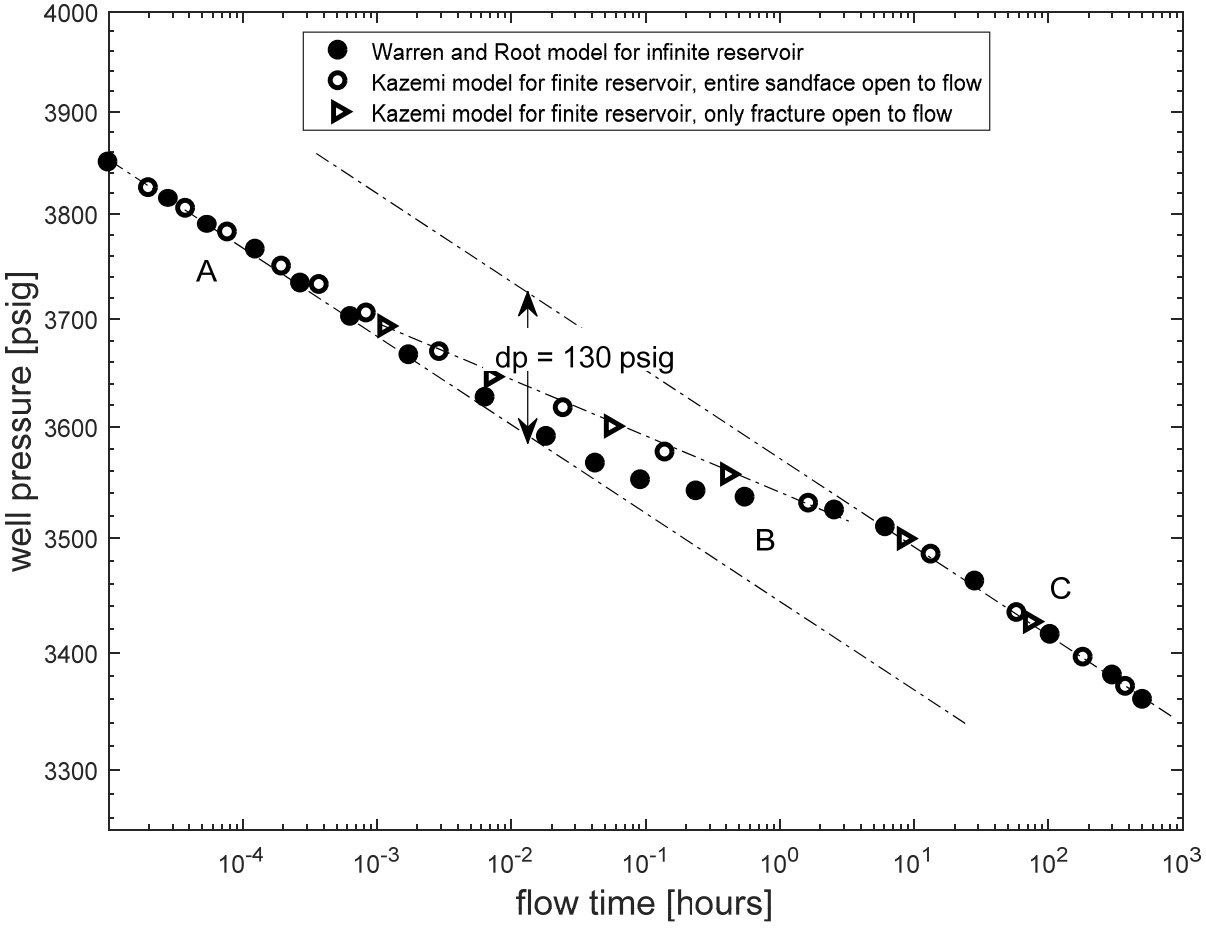


**Figure 2**

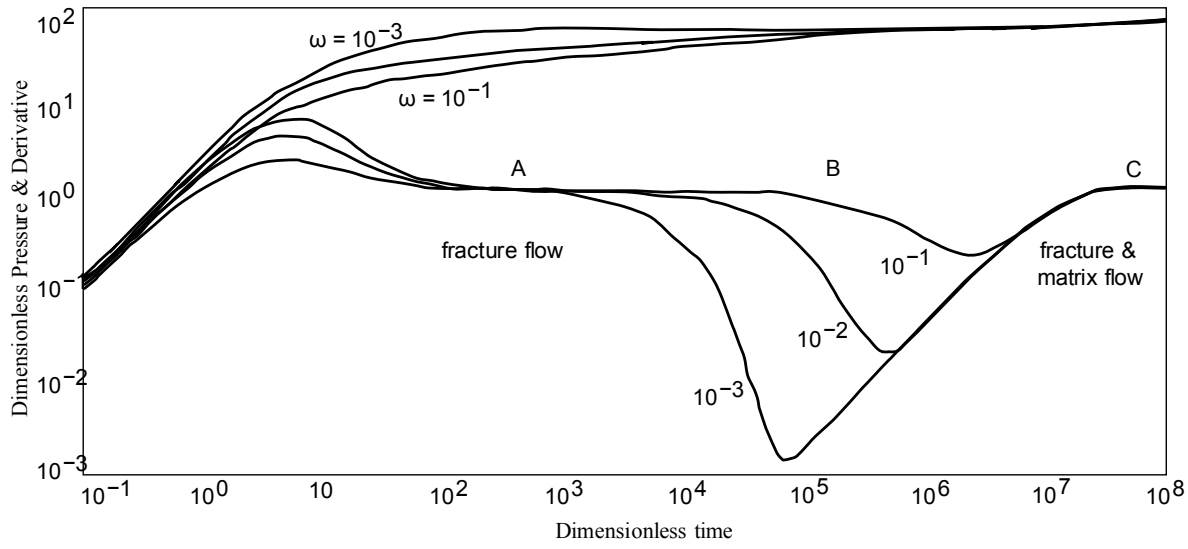


**Figure 3**

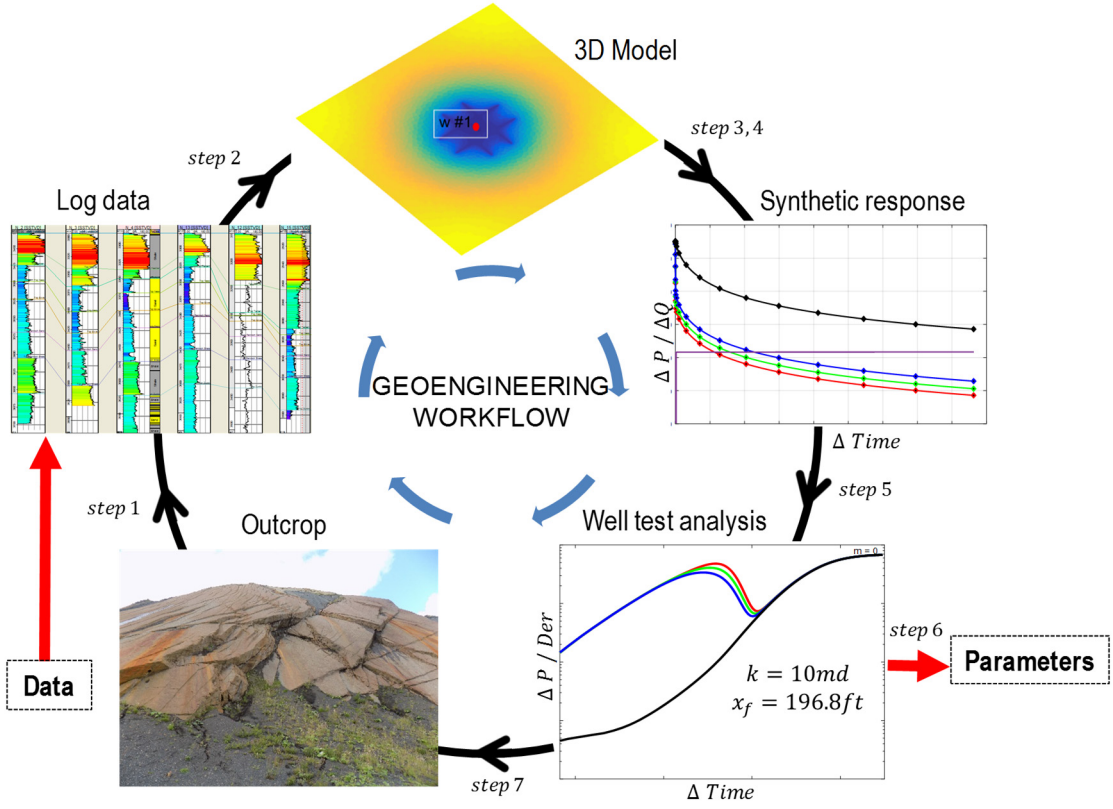


**Figure 4**

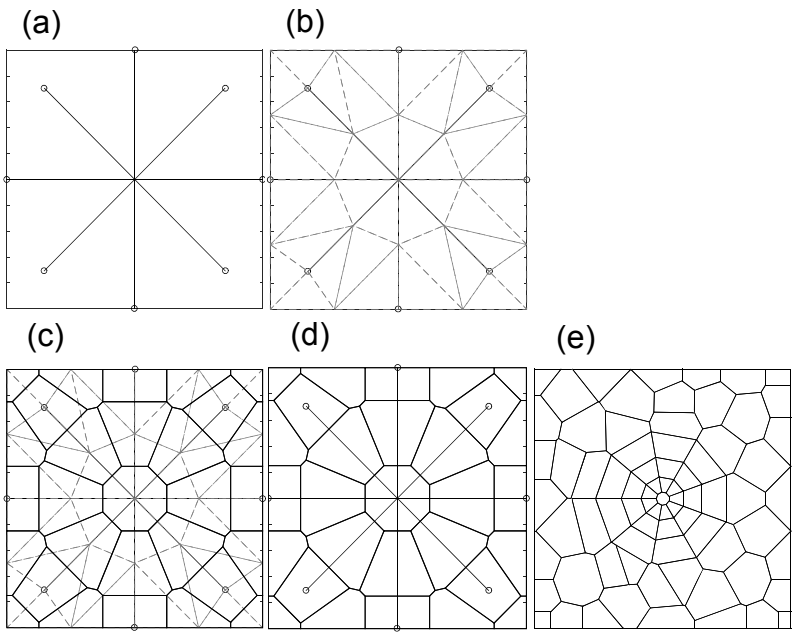


**Figure 5**

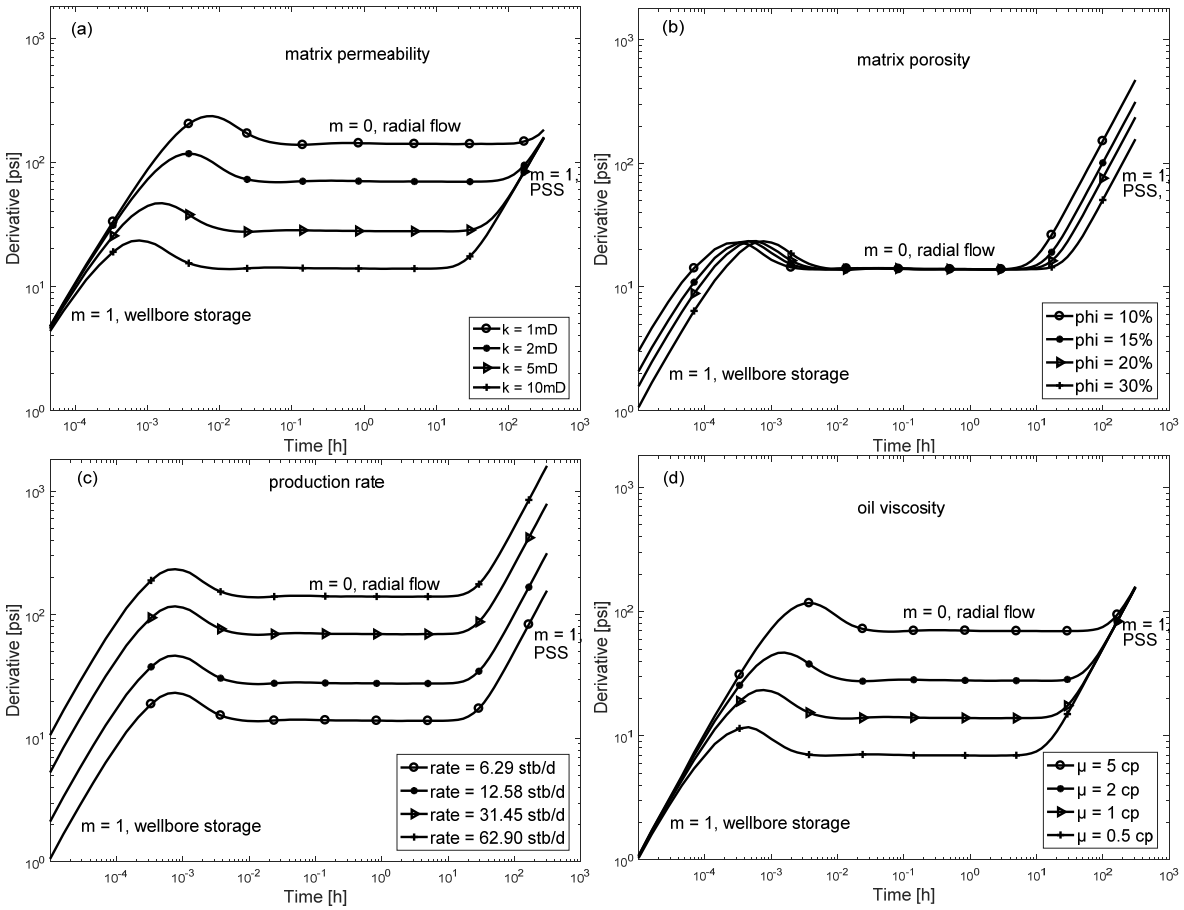


**Figure 6**

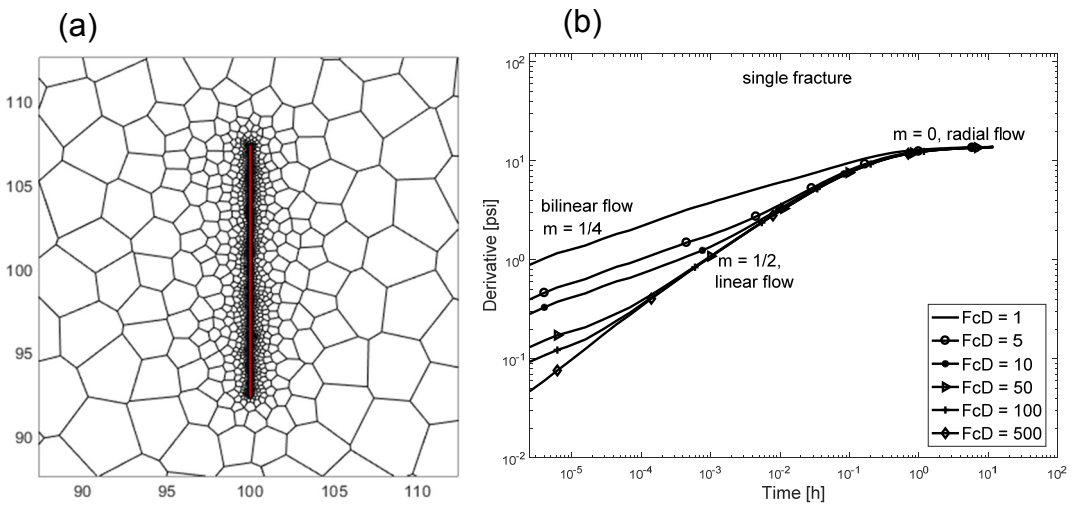


**Figure 7**

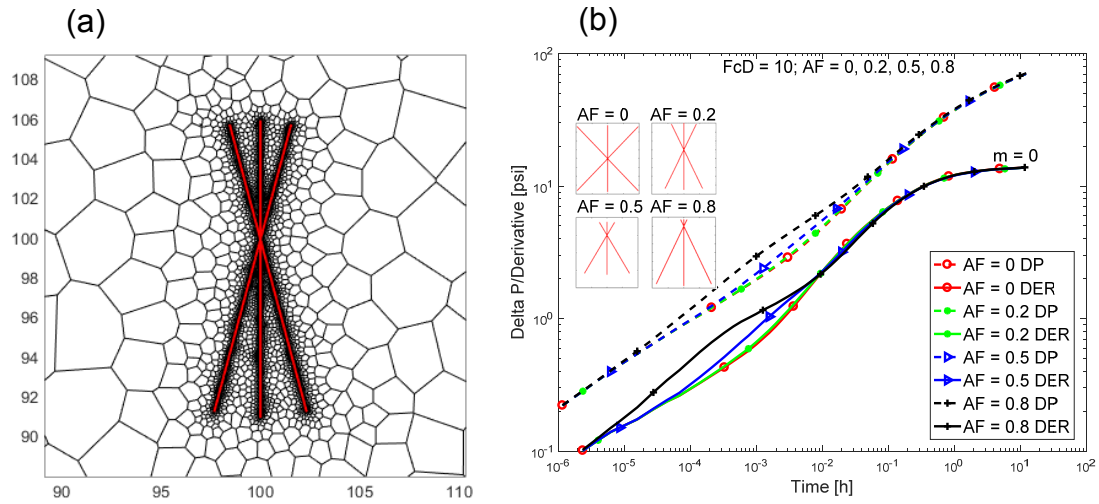


**Figure 8**

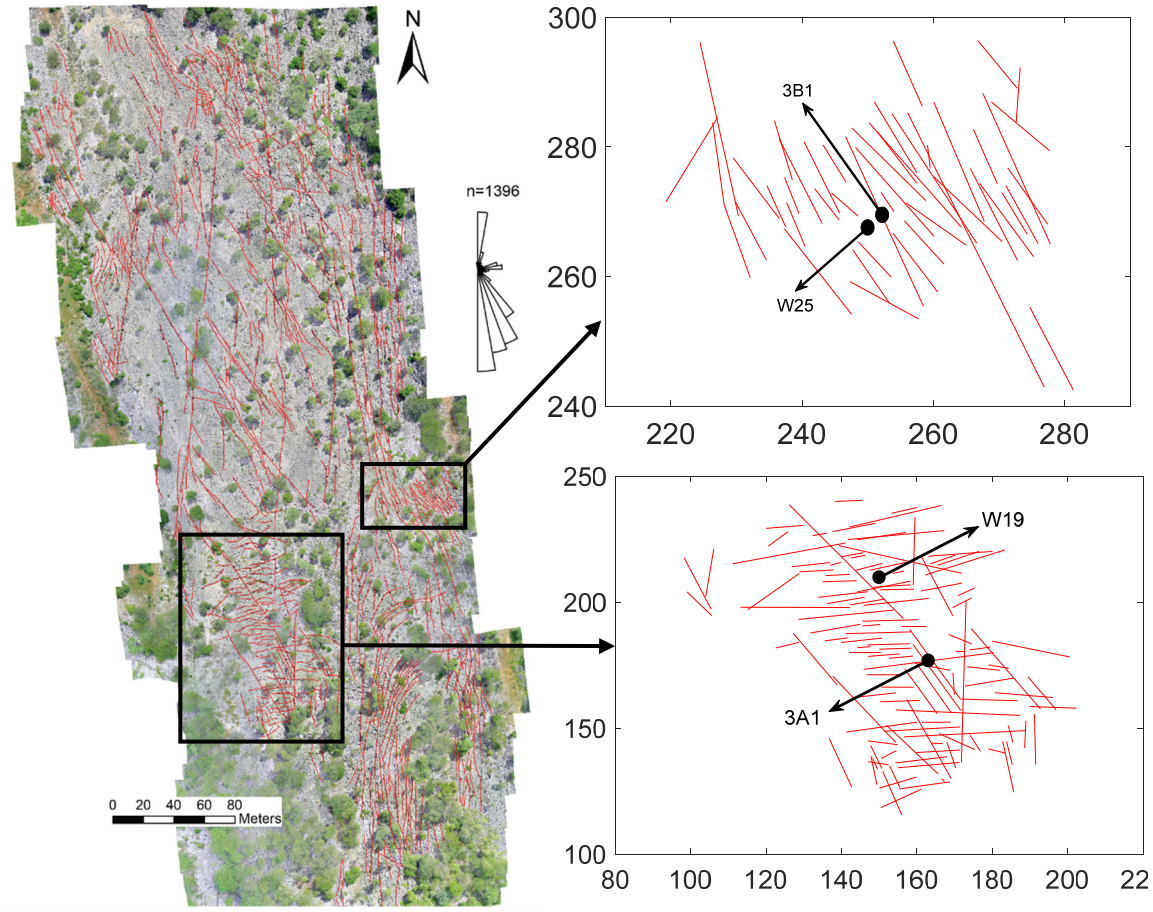


**Figure 9**

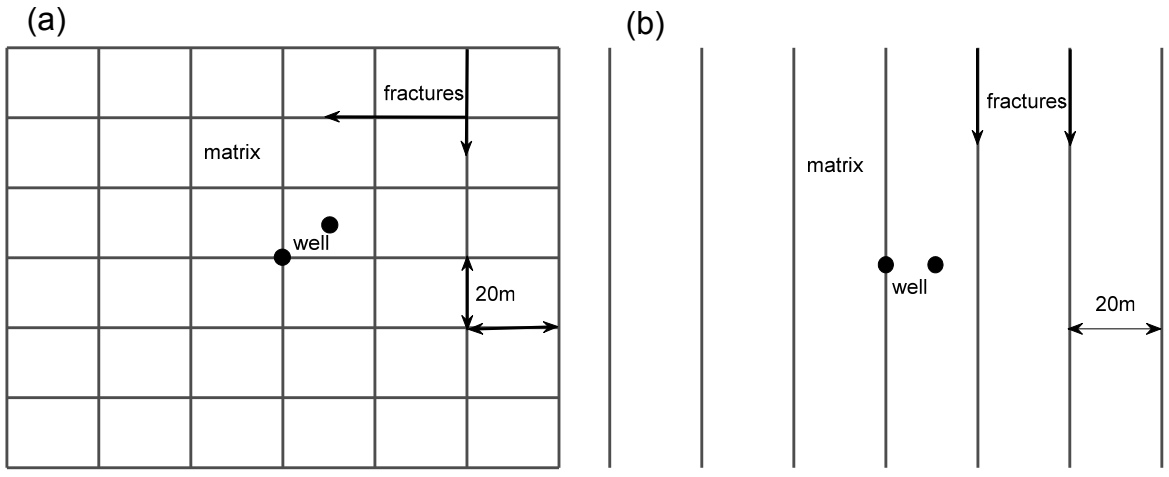


**Figure 10**

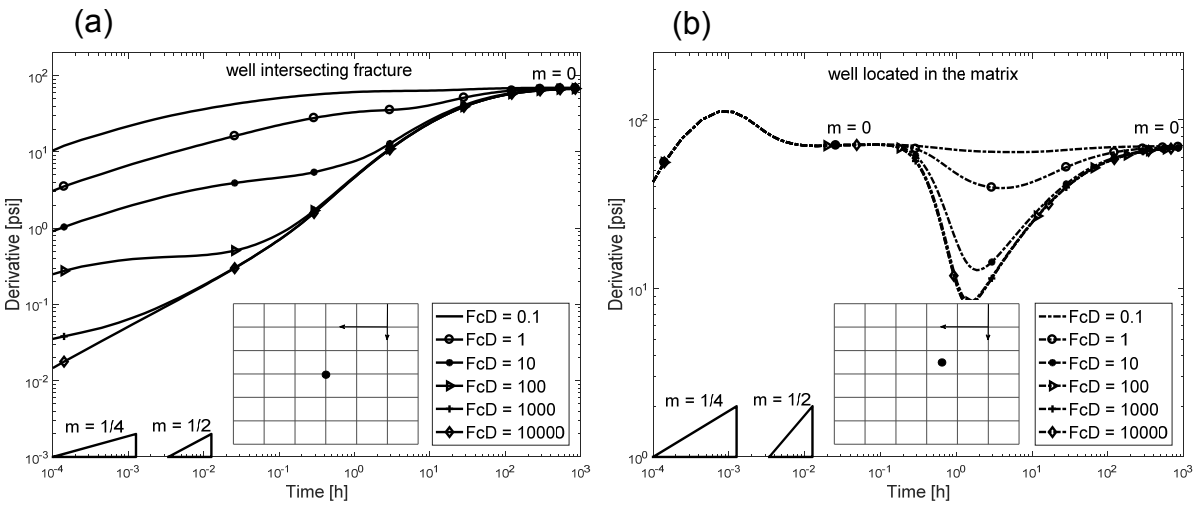


**Figure 11**

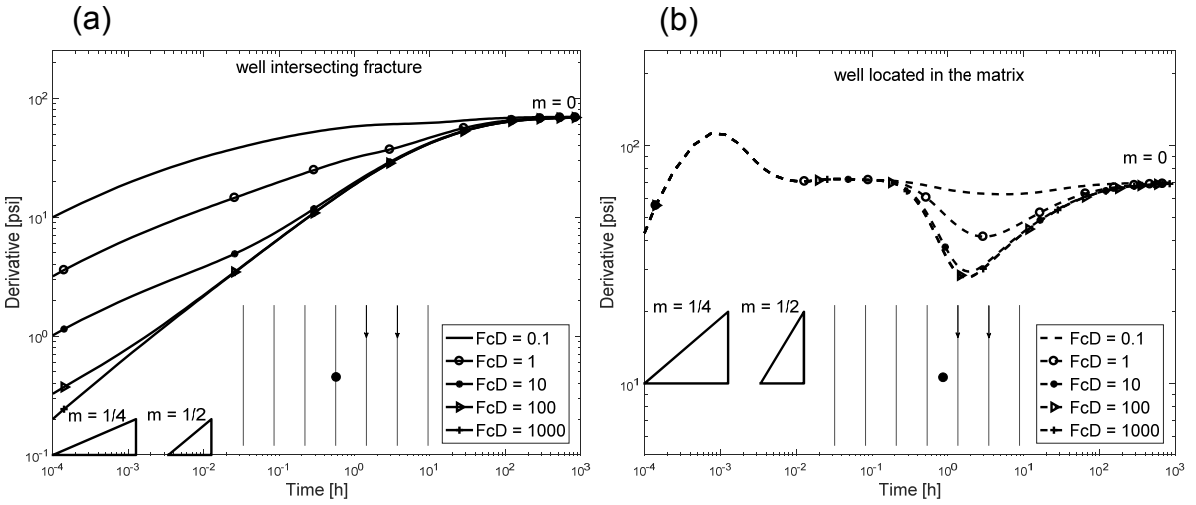


**Figure 12**

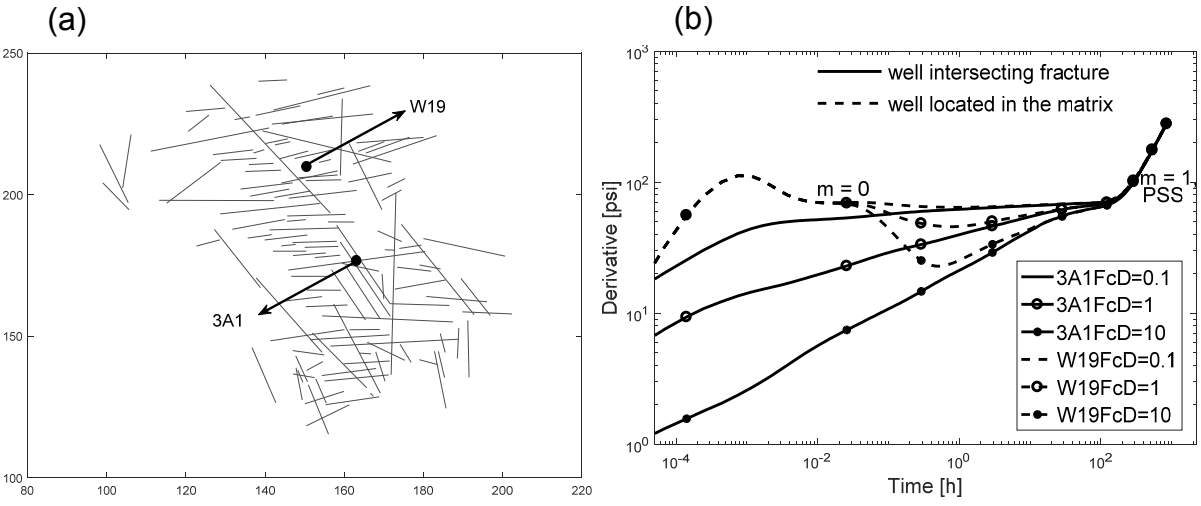


**Figure 13**

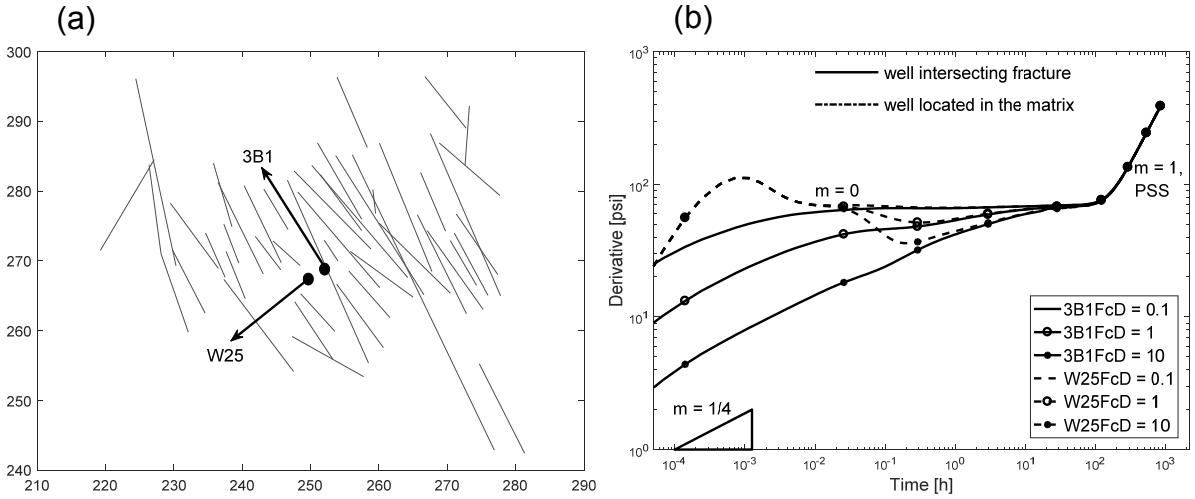


**Figure 14**

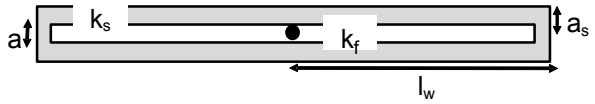


**Figure 15**

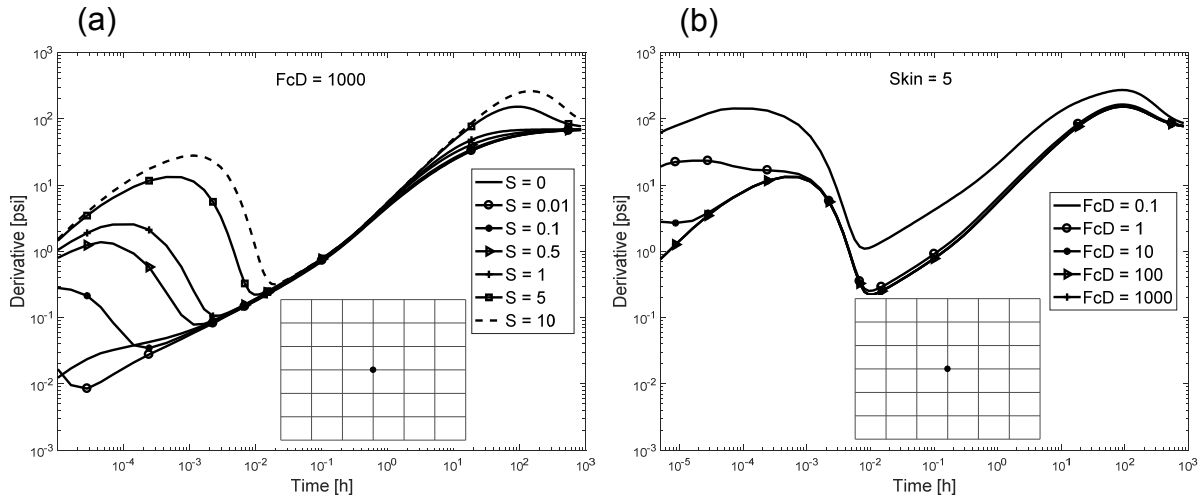


**Figure 16**

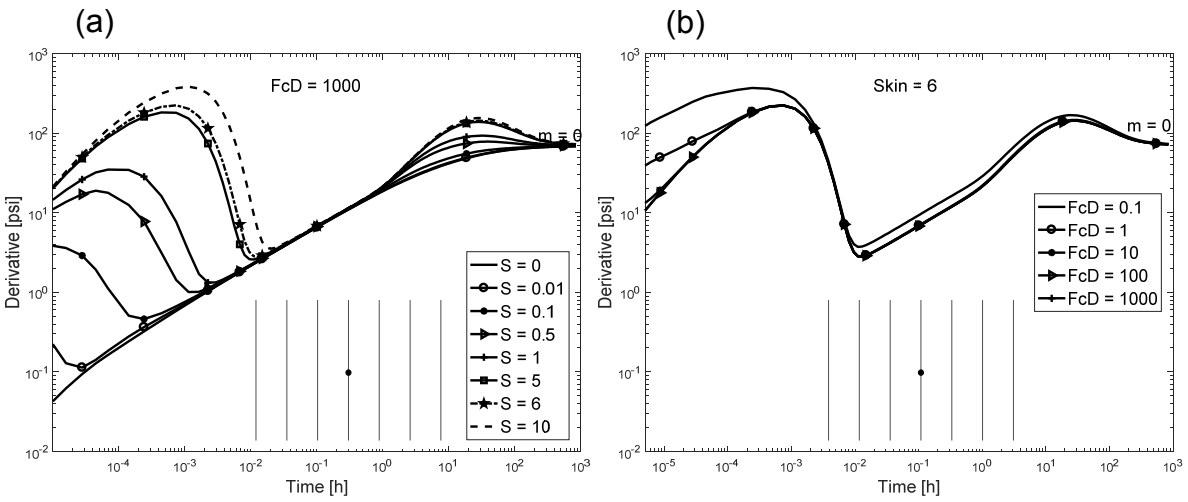


**Figure 17**

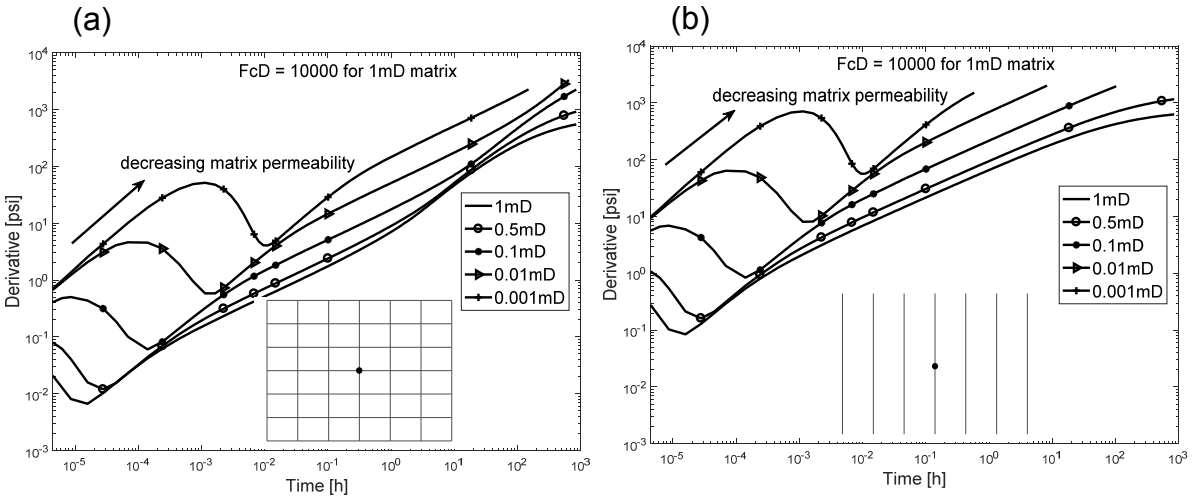


**Figure 18**

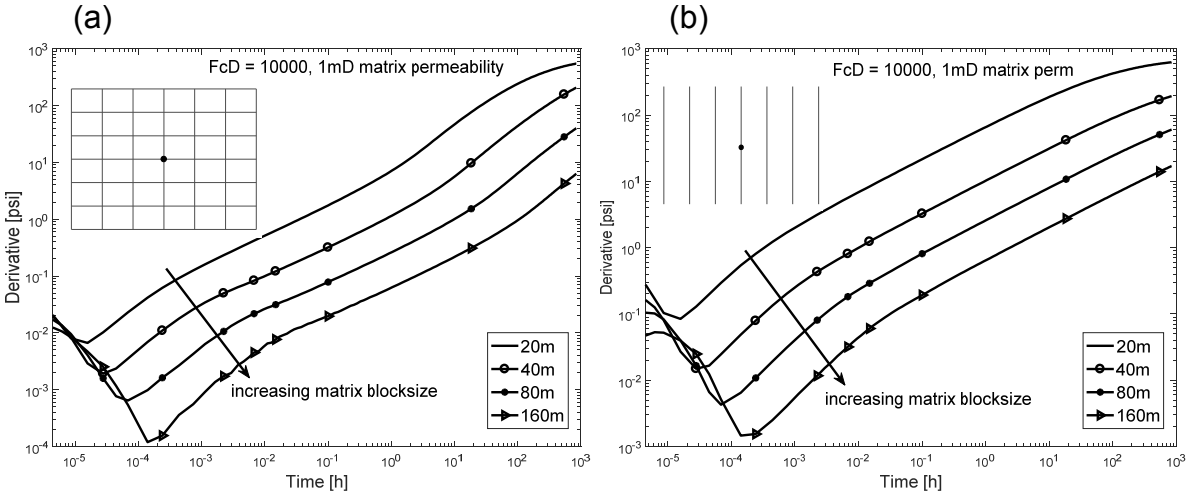


**Figure 19**

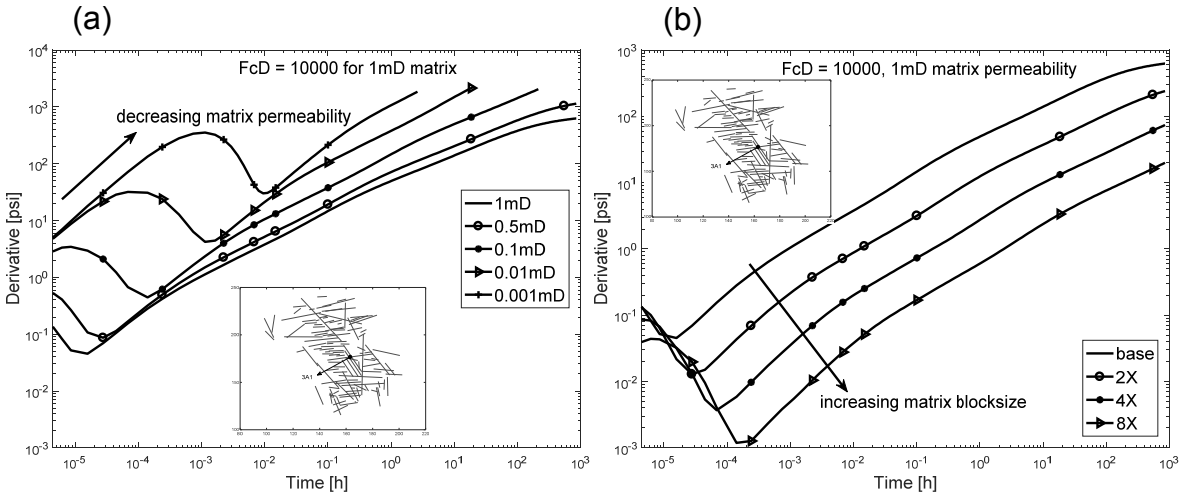


**Figure 20**

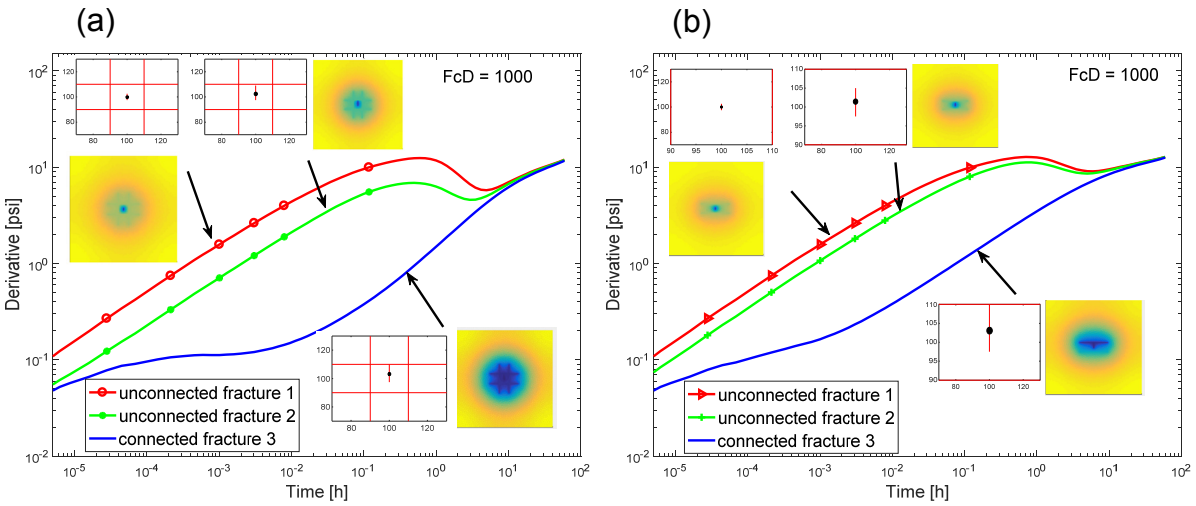


**Figure 21**

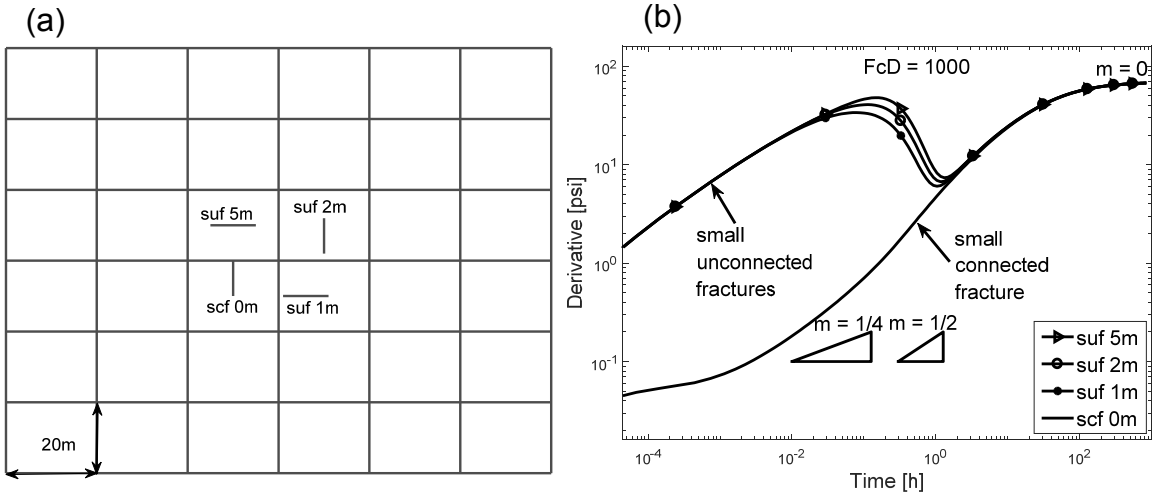

**Figure 22**

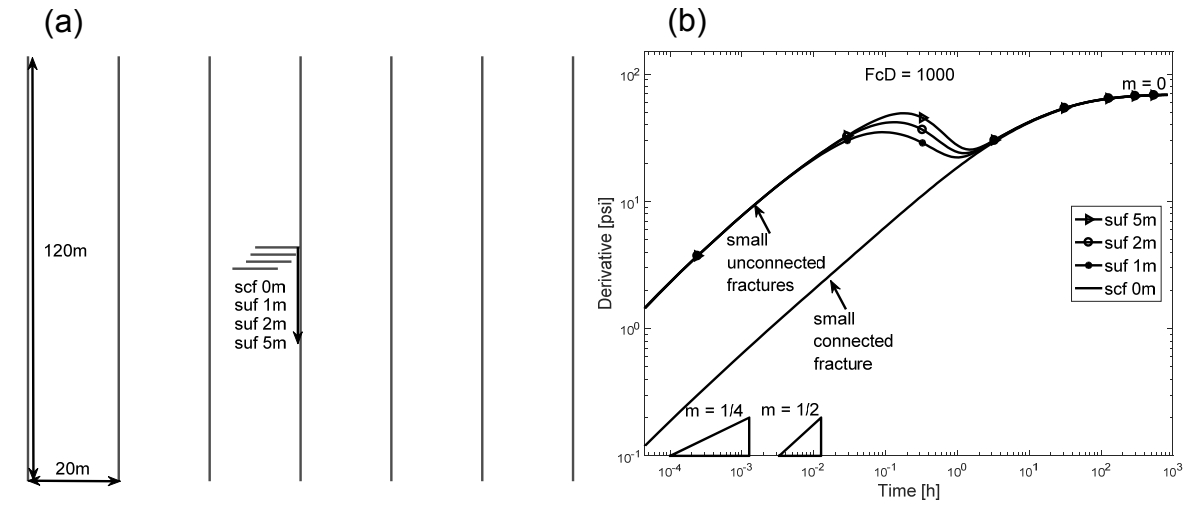


**Figure 23**

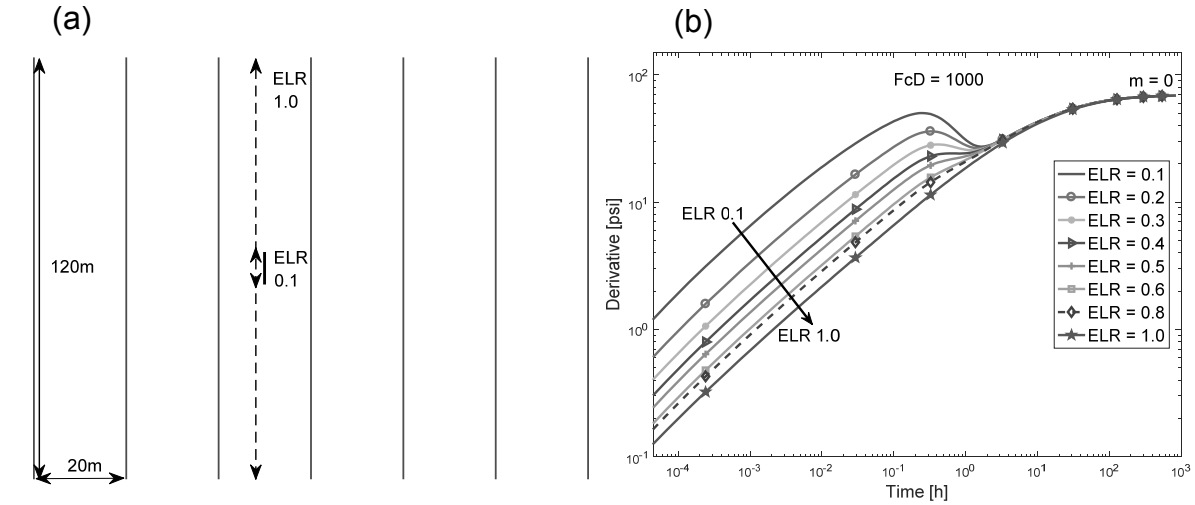


**Figure 24**

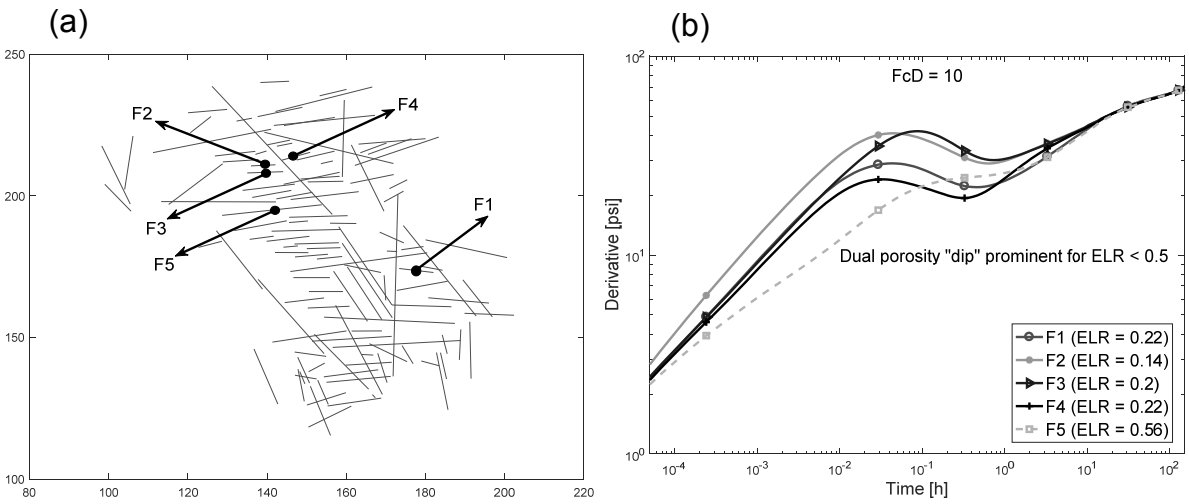
(a)
(b)
F1
F2
F3
F4
F5
FcD = 10
Dual porosity "dip" prominent for ELR < 0.5
Derivative [psi]
Time [h]
F1 (ELR = 0.22)
F2 (ELR = 0.14)
F3 (ELR = 0.2)
F4 (ELR = 0.22)
F5 (ELR = 0.56)

**Figure 25:**

**Figures captions**

**Fig. 1**: Idealisation of a dual-porosity medium. (a) Fractured and jointed carbonate reservoir image at the well test scale from the Cap Cable analogue (Barremian, Lower Cretaceous, Cassis, France) used for many carbonate fields, and (b) simulation reservoir model. (Modified from Warren & Root 1963).

**Fig. 2:** Pressure drawdown according to the model by Warren & Root and Kazemi (modified from Kazemi 1969). dp denotes vertical separation of the drawdown curve.

**Fig. 3:** Dual-porosity V-shape on a log-log plot showing influence of storativity ratio (ω) on pressure derivative. Interporosity flow coefficient ($\boldsymbol{\lambda}$) $= \mathbf{10}^{-7}$. (Modified from Bourdet 2002)

**Fig. 4:** Geoengineering workflow for integrated well testing (modified from Corbett et al. 2012).

**Fig. 5**: Mesh generation. (a) Planar straight line graph (PSLG) representing sets of fracture nodes and adjoining edges, (b) Delaunay triangulation (grey dash lines), (c) PEBI grids built around triangular mesh nodes, (d) resulting PEBI with respect to initial PSLG, and (e) separate meshing example showing radial gridding around a well.

**Fig. 6**: Un-fractured (matrix) model sensitivities. (a) Matrix permeability, (b) matrix porosity, (c) production rate, and (d) oil viscosity.

**Fig. 7**: Single fracture model. (a) Close-up of the unstructured PEBI grid with refinement around a single fracture, and (b) simulated results with variable fracture conductivities (FcD of 1 to 500). FcD denotes dimensionless fracture conductivity as defined in equation 4.

**Fig. 8**: Multiwing fractures model. (a) Close-up of the unstructured PEBI grid with refinement around multiwing fractures, and (b) simulated results with FcD of 10, AF of 0 to 0.8. The dashed lines and solid lines show changes in pressure and the corresponding pressure derivatives respectively. Asymmetry factor, AF, measures the well offset from the centre of the fracture.

**Fig. 9**: Aerial view of the fracture patterns in the Jandaira formation, Brazil (left). Marked inset boxes indicate locations where subset-models fractures patterns are taken. The upper inset to represent disconnected fracture and network and the lower inset for connected fracture network.

**Fig. 10**: Idealised fracture network with 60m half-length. (a) Connected fracture network with well intersecting fractures and located in the matrix adjacent to fractures, and (b) disconnected fracture network with similar well configurations to (a).

**Fig. 11**: Simulated pressure derivatives of an idealised connected fracture network that resembles the classical Warren and Root (1963) dual-porosity model in 2D. (a) Wellbore intersecting fractures, and (b) wellbore located in the matrix adjacent to fractures. m indicates the slope of the pressure derivative. Note that a slope, m of 0 shows radial flow or pseudo-radial flow, m of 1/2 shows formation linear flow and m of 1/4 shows bilinear flow.

**Fig. 12**: Simulated pressure derivatives of an idealised disconnected fracture network with variable dimensionless fracture conductivities. (a) Wellbore intersecting fractures, and (b) wellbore located in the matrix adjacent to fractures. m indicates the slope of the pressure derivative. Note that a slope, m of 0 shows radial or pseudo-radial flow, m of 1/2 shows formation linear flow and m of 1/4 shows bilinear flow.

**Fig. 13**: Model of a connected fracture network located in Jandaira formation (Fig. 9 lower inset): (a) Fracture network with locations of wells (unit is in metres), and (b) simulated pressure derivatives. Solid lines represent simulations for well intersecting fracture and dashed lines for well located in the matrix. Note that a slope, m of 0 shows radial flow and m of 1 shows reservoir boundary.

**Fig. 14**: Model of a disconnected fracture network located in Jandaira formation (Fig. 9 upper inset): (a) fracture network with locations of wells (unit is in metres), and (b) simulated pressure derivatives. Solid lines represent simulations for well intersecting fracture and dashed line for well located in the matrix. Note that a slope, m of 0 shows radial flow, m of 1 shows reservoir boundary and m of 1/4 shows bilinear flow.

**Fig. 15**: Diagram illustrating fracture skin surrounding a single fracture penetrated by a wellbore at half-length, $\boldsymbol{l_w}$. $\boldsymbol{a}$, $\boldsymbol{k_f}$, $\boldsymbol{a_s}$ $\boldsymbol{and}$ $\boldsymbol{k_s}$ denote fracture aperture, fracture permeability, damage (skin) zone aperture and skin zone permeability respectively.

**Fig. 16**: Simulated pressure derivatives of a fracture intersecting well in an idealised connected fracture network. (a) Variable skin (S of 0 to 10) with FcD of 1000, and (b) constant skin of 5 with variable fracture conductivities (FcD of 0.1 to 1000).

**Fig. 17**: Simulated pressure derivatives of a fracture intersecting well in an idealised disconnected fracture network. (a) Variable skin (S of 0 to 10) with FcD of 1000, and (b) constant skin of 6 with variable fracture conductivities (FcD of 0.1 to 1000).

**Fig. 18**: Simulated pressure derivatives of well intersecting fractures in idealised fracture networks with a matrix permeability ranging from 1 to 0.001mD for a connected fracture network (a), and disconnected fractures (b).

**Fig. 19**: Simulated pressure derivatives of well intersecting fracture(s) in idealised fracture networks with increasing matrix block size from 20 to 160m at a constant matrix permeability of 1mD for a connected fracture network (a), and disconnected fractures (b).

**Fig. 20**: Simulated pressure derivative of well intersecting fractures in an outcrop fracture pattern with (a) decreasing matrix permeability ranging from 1 to 0.001mD, and (b) increasing matrix block size up to a factor of 8.

**Fig. 21**: Idealised models showing fracture geometry, simulated isobars around the well and pressure derivatives of smaller (un)connected fractures close to large fractures for a connected fracture network (a), and disconnected fracture network (b).

**Fig. 22**: Well intersecting smaller (un)connected fractures in an idealised connected fracture network. Fracture geometry with 5m, 2m and 1m separation distance between smaller fractures and the large fractures (a), and simulated pressure derivatives of the configurations shown (b).

**Fig. 23**: Well intersecting smaller (un)connected fractures in an idealised disconnected fracture network. Fracture geometry with 5m, 2m and 1m separation distance between smaller fractures and the large fractures (a), and simulated pressure derivatives of the configurations shown (b).

**Fig. 24**: Well intersecting smaller unconnected fracture in an idealised disconnected fracture network. Fracture geometry with increasing length (ELR of 0.1 to 1) of a smaller fracture located close to large fractures (units in metres) (a), and simulated pressure derivatives of the configurations shown (b). ELR is effective length ratio defined in equation (8).

**Fig. 25:** Well intersecting smaller unconnected fractures located in Jandaira formation (Fig. 9 lower inset). Fracture geometry with variable lengths of fractures and separation distances between smaller fractures and the large fractures (a), and simulated pressure derivatives of the configurations shown (b).